Final Report
National Aeronautics and Space Administration
Lewis Research Center
Grant NSG-3101

MEASUREMENTS OF MIXED-MODE CRACK SURFACE DISPLACEMENTS AND COMPARISON WITH THEORY

prepared by:

Nicholas J. Altiero, Jr.
William N. Sharpe, Jr.
Michigan State University

Division of Engineering Research
Michigan State University
East Lansing, Michigan 48824
September 5, 1978

Final Report
National Aeronautics and Space Administration
Lewis Research Center
Grant NSG-3101

MEASUREMENTS OF MIXED-MODE CRACK SURFACE DISPLACEMENTS AND COMPARISON WITH THEORY

prepared by:

Nicholas J. Altiero, Jr.
William N. Sharpe, Jr.
Michigan State University

Division of Engineering Research
Michigan State University
East Lansing, Michigan 48824
September 5, 1978

TABLE OF CONTENTS

MEASUREMENTS OF MIXED-MODE CRACK SURFACE DISPLACEMENTS AND COMPARISON WITH THEORY

1. INTRODUCTION

The general problem of mixed mode crack extension has received relatively little attention until quite recently. The main effort of investigators to date has been toward development of a criterion of fracture for combined modes I and II. It has been proposed that this criterion is a functional relationship between mode I and mode II stress intensity factors which can be equated to the strain energy release rate or strain energy density at fracture. Practical application of such a criterion is limited, however, by a lack of knowledge of these properties for specific materials, geometries, and loadings. Thus, mixed mode fracture mechanics has reached the level at which classical fracture mechanics was fifteen years ago--the level at which it is imperative that an effective method be developed for determination of the properties required for implementation of the fracture criterion. Efforts have been made to employ photoelasticity to this end, but this method suffers serious limitations, particularly in the vicinity of the crack tips.

In this report two techniques, one theoretical and the other experimental, are used to determine crack surface displacements under mixed-mode conditions. Crack surface displacements have been proven to be quite useful in mode I fracture analysis in that they are directly related to strain energy release rate and stress intensity factor. It is felt that similar relationships can be developed for the mixed-mode case.

In Section 2, a boundary-integral method is developed for application to two-dimensional fracture mechanics problems. This technique is applied

to the mixed-mode problem in Section 3. In Section 4, a laser interferometry technique, for measurement of crack surface displacements under mixed-mode conditions, is presented. The experimental measurements are reported in Section 5. Finally, in Section 6, the results of the two approaches are compared and discussed.

2. THEORETICAL APPROACH

In this section, an indirect boundary-integral equation method is presented. The basic equations of this method are first formulated and it is then shown how they can be tailored for application to problems of fracture mechanics.

2.1 An Indirect Boundary-Integral Method

Consider the plane linear elasticity problem shown in Figure 2.1 where $\vec{t}$ is a specified traction at a point on boundary portion B_t and $\vec{u}$ is a specified displacement at a point on boundary portion B_u. The region bounded by contour $B = B_t + B_u$ is denoted by R. It has been shown in Reference (1) that this problem can be solved by embedding R in an infinite plane of the same material as R, see Figure 2.2, and applying an appropriate layer of body force, $\vec{p}^*$, along B. This layer of body force is chosen such that the solution in R satisfies the boundary conditions of the problem of Figure 2.1 as B is approached from the inside. Note that the stress and displacement components at a point Z in R can be written as

$$\sigma_{ij}(Z) = \oint_B H_{ij;q}(Z,Z_o)p^*_q(Z_o)ds(Z_o)$$
$$u_i(Z) = \oint_B I_{i;q}(Z,Z_o)p^*_q(Z_o)ds(Z_o) \qquad (2.1)$$

where Z_o is a point on B and s is a coordinate measured along B. The influence functions $H_{ij;q}(Z,Z_o)$ and $I_{i;j}(Z,Z_o)$ are the ij-th stress component and the i-th displacement component, respectively, at Z in an infinite plane caused by a unit load in the q-th direction applied at Z_o. Since this solution must satisfy the appropriate boundary

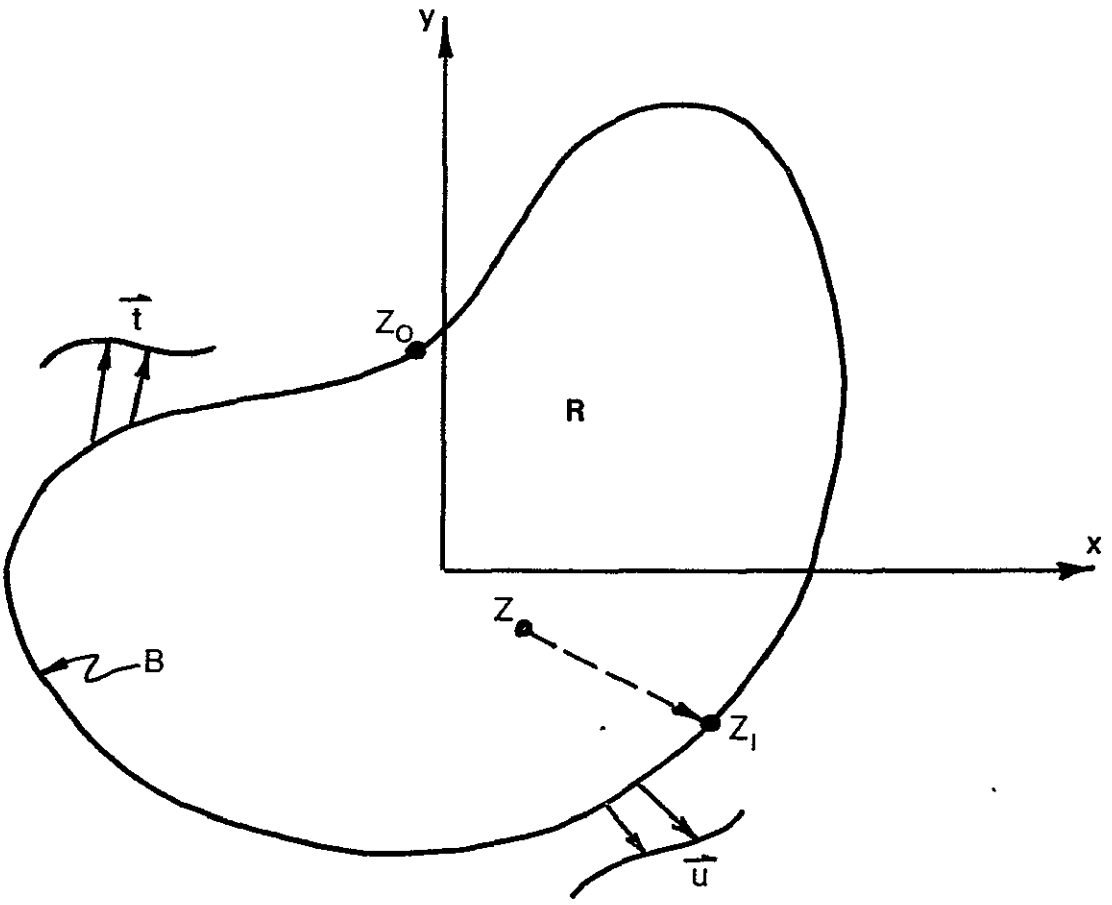

Figure 2.1. Boundary-Value Problem Involving Simply-Connected Region.

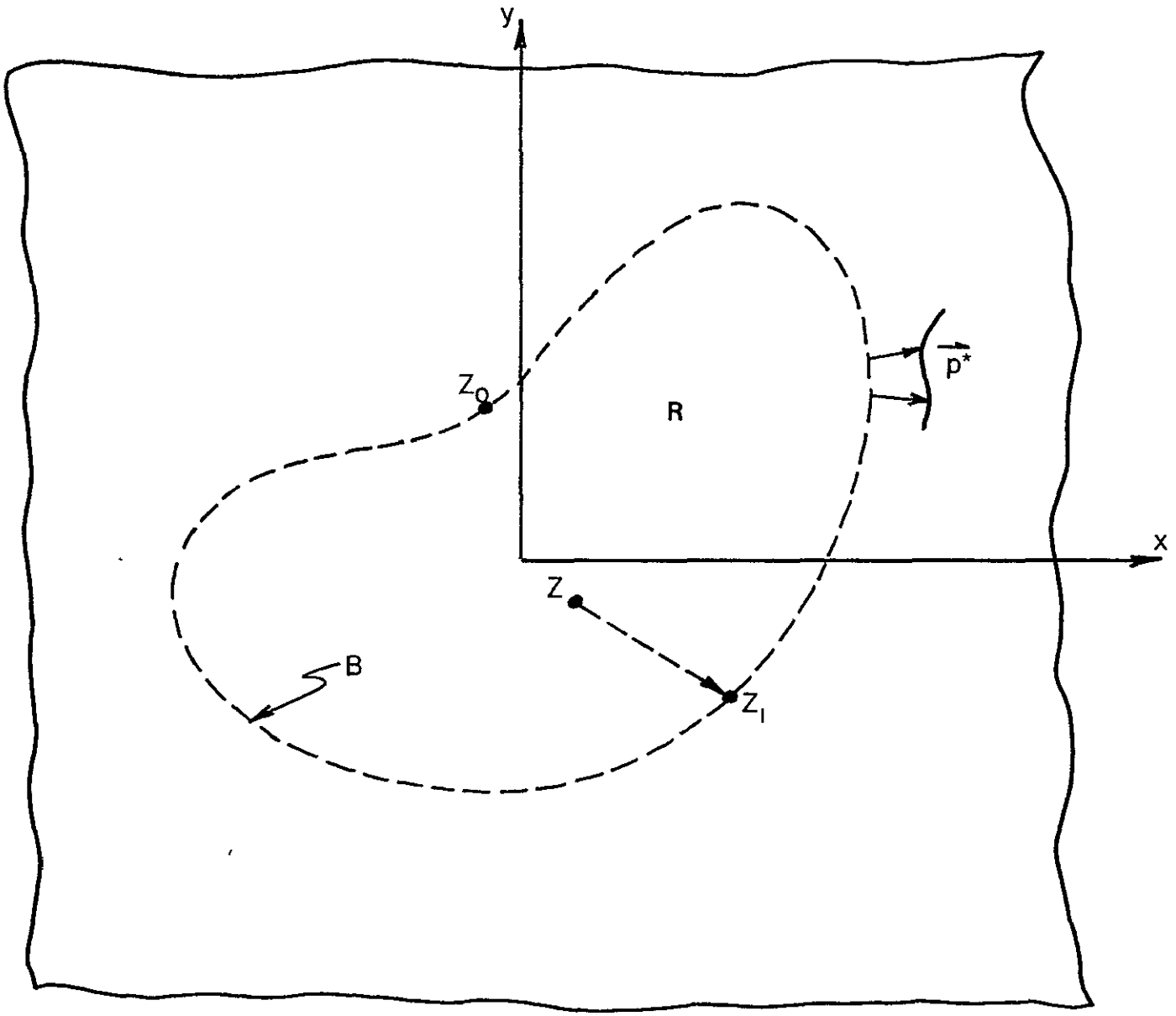

Figure 2.2. Simply-Connected Region Embedded in Infinite Plane and Subjected to Layer of Body Force.

conditions as Z approaches a point Z_1 on B from the inside, then $\vec{p}^*$ must be chosen such that

$$\frac{1}{2} p^*_i(Z_1) + \oint_B H_{ij;q}(Z_1,Z_o) p^*_q(Z_o) n_j(Z_1) ds(Z_o) = t_i(Z_1)$$

$$Z_1 \text{ on } B_t \qquad (2.2)$$

$$\oint_B I_{i;q}(Z_1,Z_o) p^*_q(Z_o) ds(Z_o) = u_i(Z_1)$$

$$Z_1 \text{ on } B_u$$

where the integral in the first equation is to be interpreted in the sense of the Cauchy principal-value.

The solution to a particular problem can be obtained by discretizing the boundary and the boundary-values and converting Eqs. (2.1) and (2.2) to linear algebraic equations. Consider, for example, the traction boundary-value problem, i.e., $B = B_t$, in which the right-hand side of the first of Eqs. (2.2), i.e., $\vec{t}(Z_1)$, is known. Suppose that B is divided into N intervals of length ΔS_k, $k = 1,\ldots,N$, and let the traction of Figure 2.1 and the body force layer of Figure 2.2 be integrated over interval ΔS_k, denoting the resultants as

$$P_{ik} = \int_{\Delta S_k} t_i ds \qquad P^*_{ik} = \int_{\Delta S_k} p^*_i ds \qquad (2.3)$$

where $i = x,y$; $k = 1,\ldots,N$. If these resultant forces are then located at the centerpoint of interval ΔS_k, the boundary-integral equations are converted to

$$\frac{1}{2} P^*_{i\ell}(Z_1) + \sum_{\substack{k=1 \\ k\neq\ell}}^{N} H_{ij;q}(Z_1,Z_o) P^*_{qk}(Z_o) n_j(Z_1) \Delta S_\ell = P_{i\ell}(Z_1) \qquad (2.4)$$

$$i=x,y;\ j=x,y;\ \ell=1,\ldots,N$$

where Z_1 is the centerpoint of the ℓ-th boundary subdivision and

Z_o is the centerpoint of the k-th boundary subdivision. Once this 2N X 2N system of equations is solved for P^*_{ik}, i=x,y, k=1, ...,N, the stress and displacement components at any field point Z in R can be found by simple summation:

$$\sigma_{ij}(Z) = \sum_{k=1}^{N} H_{ij;q}(Z,Z_o)P^*_{qk}(Z_o) \tag{2.5}$$

$$u_i(Z) = \sum_{k=1}^{N} I_{i;q}(Z,Z_o)P^*_{qk}(Z_o)$$

The influence functions in Eqs. (2.4) and (2.5) can be written in terms of the complex potential functions, φ and ψ, associated with an infinite plane subjected to a point load $P^*_k(Z_o) = P^*_{xk}(Z_o) + iP^*_{yk}(Z_o)$ applied at a point Z_o, see Reference (2):

$$\begin{aligned}
H_{xx;q}(Z,Z_o)P^*_{qk}(Z_o) &= R\ell[2\varphi'(Z,Z_o) - \bar{Z}\varphi''(Z,Z_o) - \psi'(Z,Z_o)] \\
H_{yy;q}(Z,Z_o)P^*_{qk}(Z_o) &= R\ell[2\varphi'(Z,Z_o) + \bar{Z}\varphi''(Z,Z_o) + \psi'(Z,Z_o)] \\
H_{xy;q}(Z,Z_o)P^*_{qk}(Z_o) &= H_{yx;q}(Z,Z_o)P^*_{qk}(Z_o) \\
&= Im[\bar{Z}\varphi''(Z,Z_o) + \psi'(Z,Z_o)]
\end{aligned} \tag{2.6}$$

$$\begin{aligned}
I_{x;q}(Z,Z_o)P^*_{qk}(Z_o) &= \frac{1}{2\mu} R\ell[\alpha\varphi(Z,Z_o) - Z\overline{\varphi'(Z,Z_o)} - \overline{\psi(Z,Z_o)}] \\
I_{y;q}(Z,Z_o)P^*_{qk}(Z_o) &= \frac{1}{2\mu} Im[\alpha\varphi(Z,Z_o) - Z\overline{\varphi'(Z,Z_o)} - \overline{\psi(Z,Z_o)}]
\end{aligned}$$

where

$$\alpha = \begin{cases} \dfrac{3-\nu}{1+\nu} & \text{plane stress} \\ 3 - 4\nu & \text{plane strain} \end{cases}$$

and μ,ν are the shear modulus and Poisson's ratio respectively. The complex potential functions in Eqs. (2.6) can be expressed as

$$\varphi(Z,Z_o) = \varphi^o(Z,Z_o) + \varphi^*(Z,Z_o)$$
$$\psi(Z,Z_o) = \psi^o(Z,Z_o) + \psi^*(Z,Z_o) \qquad (2.7)$$

where $\varphi^*(Z,Z_o) = \psi^*(Z,Z_o) = 0$ and

$$\varphi^o(Z,Z_o) = -\frac{P^*_k(Z_o)}{2\pi(\alpha+1)}\ \ell n(Z-Z_o)$$
$$\psi^o(Z,Z_o) = \alpha\frac{\overline{P^*_k(Z_o)}}{2\pi(\alpha+1)}\ \ell n(Z-Z_o) + \frac{P^*_k(Z_o)}{2\pi(\alpha+1)}\ \frac{\bar{Z}_o}{Z-Z_o} \qquad (2.8)$$

Note again that, in the context of the boundary-value problem of interest, Z_o is to be interpreted as the centerpoint of the k-th boundary subdivision.

Results obtained by this method have been shown to be quite good everywhere in R except in a region close to B, i.e., close to the discretization. This is usually not a severe limitation but it would be a major shortcoming if one wanted to examine the solution in the vicinity of a hole, as in the problem of Figure 2.3. Note that one could treat the problem of Figure 2.3 in the manner described above by simply considering the integrals to be taken over boundary B + C. However, solutions in the vicinity of the hole boundary, C, would be adversely affected by the subsequent discretization. A procedure will now be presented which remedies this situation.

2.2 The B.I.E. Method Applied to Fracture Mechanics

The technique developed here is also presented in Reference (3).

Suppose that one knows the complex potential functions, φ and ψ, for an infinite plane containing the hole of contour C and subjected to the load $P^*_k(Z_o)$ applied at Z_o, see Figure 2.4(a). Then it is clear that the problem of Figure 2.3 can be solved by embedding the region of Figure 2.3 in the region of Figure 2.4(a) with

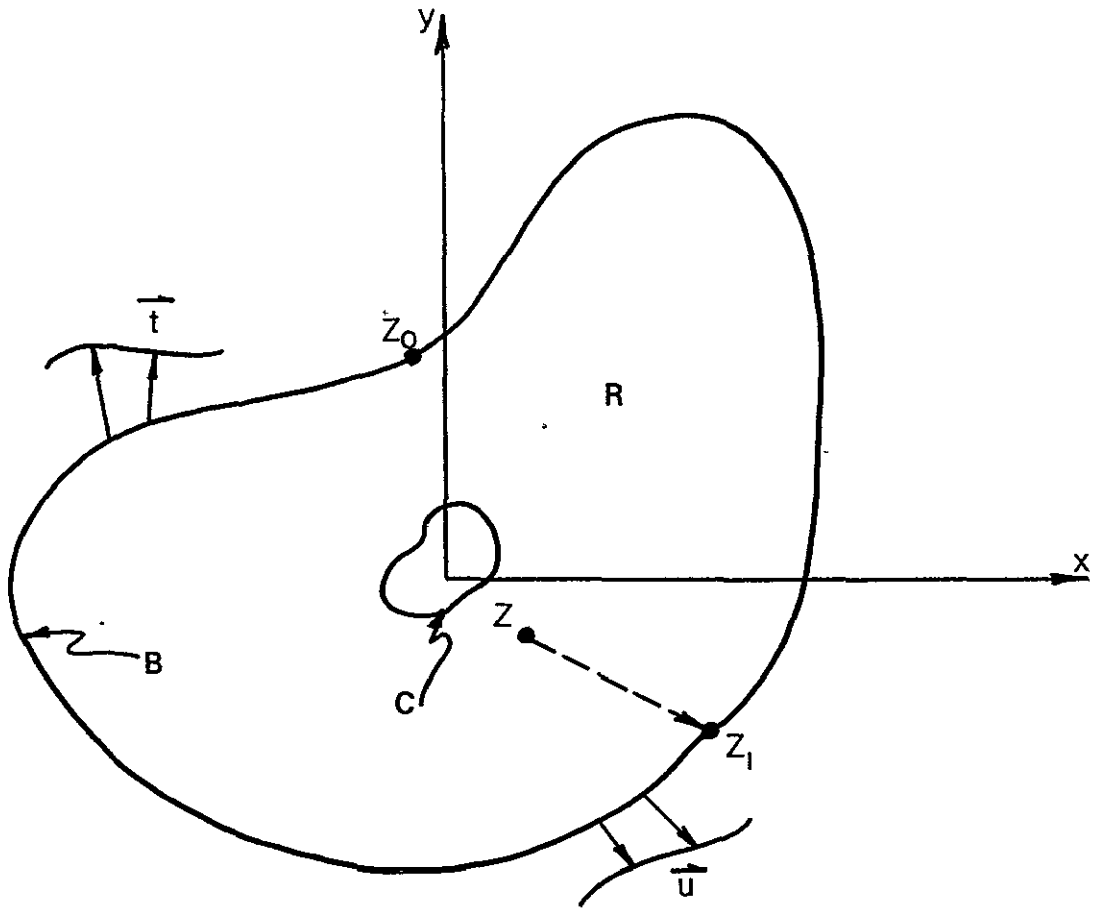

Figure 2.3. Boundary-Value Problem Involving Region Weakened by Hole.

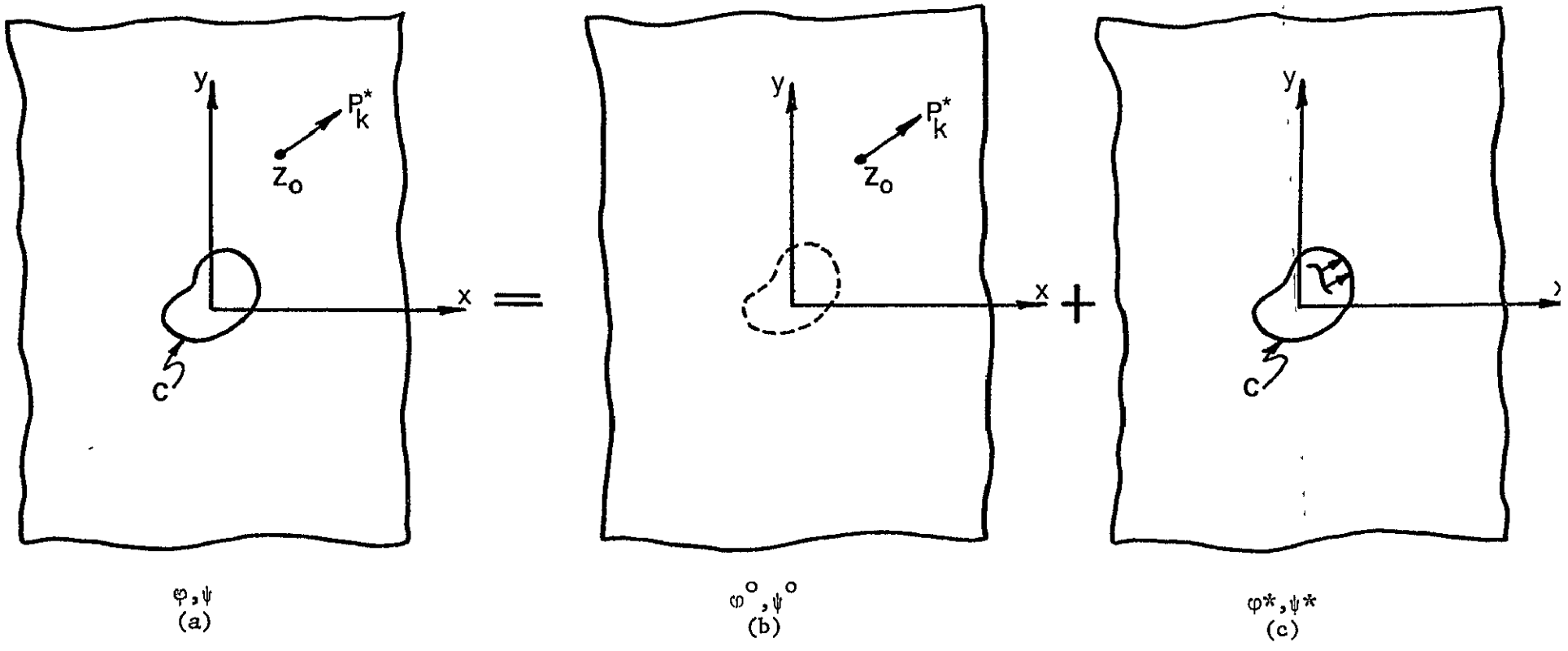

Figure 2.4. Fundamental Solution Containing Hole, Expressed as Superposition of Two Problems.

contour B properly oriented relative to the hole. Then the solution to the problem of Figure 2.3 is contained in Eqs. (2.4)-(2.8) where φ^*, ψ^* are no longer zero but are the complex potential functions associated with the problem of Figure 2.4 (c), i.e., an infinite plane containing the hole of contour C, subjected to traction along C which is equal in magnitude and opposite in direction to the traction generated along an imagined contour C in the problem of Figure 2.4 (b). Thus when the solutions to the problems of Figures 2.4 (b) and 2.4 (c) are superposed, the resulting solution to the problem of Figure 2.4 (a), i.e., traction-free hole, is obtained. It can be readily shown that the boundary condition on contour C in the problem of Figure 2.4 (c) is given by:

$$\varphi^*(\tau,Z_o) + \tau\overline{\varphi^{*\prime}(\tau,Z_o)} + \overline{\psi^*(\tau,Z_o)} = [\varphi^o(\tau,Z_o) + \tau\overline{\varphi^{o\prime}(\tau,Z_o)} + \overline{\psi^o(\tau,Z_o)}] \tag{2.9}$$

where $Z = \tau$ is a point on C.

In the presentation which follows, a specific contour C will be considered, namely a sharp crack.

Consider now the problem of Figure 2.5, i.e., a plane, finite, linear elastic region, containing a sharp crack of length 2a, and subjected to a specified traction distribution on B. It is clear from the foregoing discussion that the solution to this problem can be obtained provided one can find the functions φ^* and ψ^* associated with the problem of Figure 2.4 (c) where the contour C is that of a sharp crack and the condition along C is given by Eq. (2.9). This problem can be solved in the following manner.

Note that the function which maps the infinite domain outside of C onto the unit disc is

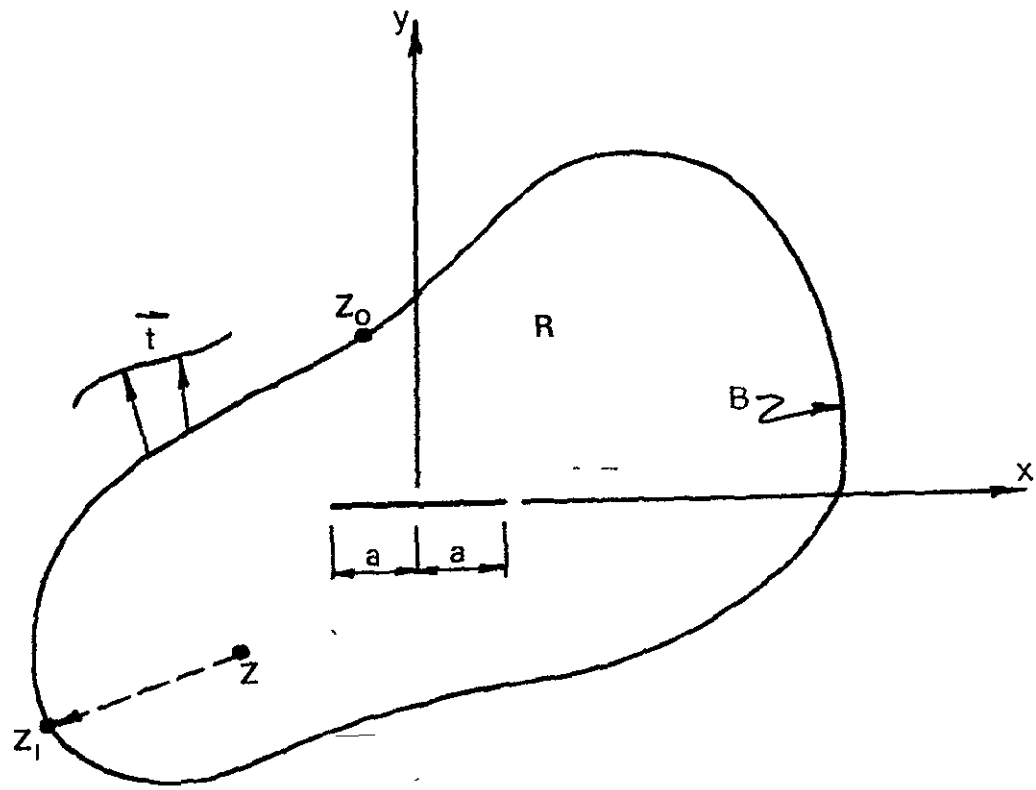

Figure 2.5. Boundary-Value Problem Involving Region Weakened by a Sharp Crack.

$$Z = \omega(\zeta) = \frac{a}{2}\left(\frac{1}{\zeta} + \zeta\right) \tag{2.10}$$

where the disc is defined in the ζ -plane.

Then

$$\varphi^*(Z) = \varphi^*[\omega(\zeta)] = \varphi_1^*(\zeta) \tag{2.11}$$

$$\psi^*(Z) = \psi^*[\omega(\zeta)] = \psi_1^*(\zeta)$$

and the condition on γ, the perimeter of the unit disc, follows from Eq. (2.9):

$$\varphi_1^*(\sigma) + \frac{\omega(\sigma)}{\omega'(\sigma)}\overline{\varphi_1^{*'}(\sigma)} + \overline{\psi_1^*(\sigma)} = F(\sigma) \tag{2.12}$$

where $\zeta = \sigma$ is a point on γ, and where

$$F(\sigma) = -[\varphi_1^{\circ}(\sigma) + \frac{\omega(\sigma)}{\omega'(\sigma)}\overline{\varphi_1^{\sigma'}(\sigma)} + \overline{\psi_1^{\circ}(\sigma)}] \tag{2.13}$$

is known.

It can be easily shown that the solution to this problem is

$$\varphi_1^*(\zeta) = \frac{1}{2\pi i}\oint_\gamma \frac{F(\sigma)}{\sigma-\zeta}\,d\sigma - \frac{1}{2\pi i}\oint_\gamma \frac{\omega(\sigma)}{\omega'(\sigma)}\frac{\overline{\varphi_1^{*'}(\sigma)}}{\sigma-\zeta}\,d\sigma \tag{2.14}$$

$$\psi_1^*(\zeta) = \frac{1}{2\pi i}\oint_\gamma \frac{\overline{F(\sigma)}}{\sigma-\zeta}\,d\sigma - \frac{1}{2\pi i}\oint_\gamma \frac{\overline{\omega(\sigma)}}{\omega'(\sigma)}\frac{\varphi_1^{*'}(\sigma)}{\sigma-\zeta}\,d\sigma$$

It is first necessary to calculate the following integrals

$$I_1 = \frac{1}{2\pi i}\oint_\gamma \frac{\omega(\sigma)}{\omega'(\sigma)}\frac{\overline{\varphi_1^{*'}(\sigma)}}{\sigma-\zeta}\,d\sigma$$
$$I_2 = \frac{1}{2\pi i}\oint_\gamma \frac{\overline{\omega(\sigma)}}{\omega'(\sigma)}\frac{\varphi_1^{*'}(\sigma)}{\sigma-\zeta}\,d\sigma \tag{2.15}$$

Since $\varphi_1^{*'}$ is analytic inside γ and $\overline{\varphi_1^{*'}}$ is analytic outside γ, one can write

$$I_1 = \frac{1}{2\pi i}\oint_\gamma \frac{1+\sigma^2}{1-\sigma^2}\frac{\sum_{k=1}^{\infty} k\bar{a}_k\sigma^{-k}}{\sigma-\zeta}\,d\sigma$$

$$I_2 = -\frac{1}{2\pi i}\oint_\gamma \frac{1+\sigma^2}{1-\sigma^2}\,\frac{\sum_{k=1}^{\infty} k a_k \sigma^{k+1}}{\sigma-\zeta}\,d\sigma \tag{2.16}$$

where the crack length, 2a, has been set equal to 4 for simplicity. Clearly Eqs. (2.16) reduce to

$$\begin{aligned} I_1 &= 0 \\ I_2 &= -\frac{\zeta(1+\zeta^2)}{1-\zeta^2}\,\varphi_1^{*\prime}(\zeta) \end{aligned} \tag{2.17}$$

Substitution of Eqs. (2.17) into Eqs. (2.14) leads to

$$\begin{aligned} \varphi_1^*(\zeta) &= \frac{1}{2\pi i}\oint_\gamma \frac{F(\sigma)}{\sigma-\zeta}\,d\sigma \\ \psi_1^*(\zeta) &= \frac{1}{2\pi i}\oint_\gamma \frac{\overline{F(\sigma)}}{\sigma-\zeta}\,d\sigma + \frac{\zeta(1+\zeta^2)}{1-\zeta^2}\,\varphi_1^{*\prime}(\zeta) \end{aligned} \tag{2.18}$$

Transforming Eqs. (2.8) to the ζ-plane and inserting the transformed functions into Eq. (2.13) yields

$$\begin{aligned} F(\sigma) = \frac{P_k^*(Z_o)}{2\pi(\alpha+1)} &\left[\ln\frac{\sigma^2-Z_o\sigma+1}{\sigma} - \alpha\ln\frac{\sigma^2-\bar{Z}_o\sigma+1}{\sigma}\right] \\ &+ \frac{\overline{P^*_k(Z_o)}}{2\pi(\alpha+1)}\,\frac{\sigma^2-Z_o\sigma+1}{\sigma^2-\bar{Z}_o\sigma+1} \end{aligned} \tag{2.19}$$

Inserting Eq. (2.19) into Eqs. (2.18):

$$\varphi_1^*(\zeta) = \frac{P_k^*(Z_o)}{4\pi^2 i(\alpha+1)}\oint_\gamma \ln\frac{(\sigma-r_i)(\sigma-r_o)}{\sigma(\sigma-\zeta)}\,d\sigma$$

$$-\frac{\alpha\overline{P_k^*(Z_o)}}{4\pi^2 i(\alpha+1)}\oint_\gamma \ln\frac{(\sigma-t_i)(\sigma-t_o)}{\sigma(\sigma-\zeta)}\,d\sigma$$

$$+\frac{P_k^*(Z_o)}{4\pi^2 i(\alpha+1)}\oint_\gamma \frac{(\sigma-r_i)(\sigma-r_o)}{(\sigma-t_i)(\sigma-t_o)(\sigma-\zeta)}\,d\sigma$$

$$\psi_1^*(\zeta) = \frac{P_k^*(Z_o)}{4\pi^2 i(\alpha+1)} \oint_\gamma \frac{(\sigma-t_i)(\sigma-t_o)}{(\sigma-r_i)(\sigma-r_o)(\sigma-\zeta)}\, d\sigma$$

$$+ \frac{\overline{P_k^*(Z_o)}}{4\pi^2 i(\alpha+1)} \oint \ell n \frac{(\sigma-t_i)(\sigma-t_o)}{\sigma(\sigma-\zeta)}\, d\sigma \qquad (2.20)$$

$$- \frac{\alpha\overline{P_k^*(Z_o)}}{4\pi^2 i(\alpha+1)} \oint_\gamma \ell n \frac{(\sigma-r_i)(\sigma-r_o)}{\sigma(\sigma-\zeta)}\, d\sigma + \frac{\zeta(\zeta^2+1)}{1-\zeta^2} \varphi_1^{*\prime}(\zeta)$$

where r_i, r_o are the roots of

$$\zeta^2 - Z_o\zeta + 1 = 0$$

inside and outside of the unit disc respectively and t_i, t_o are the roots of

$$\zeta - \overline{Z}_o\zeta + 1 = 0$$

inside and outside of the unit disc respectively. Thus

$$r_{o,i} = \frac{Z_o \pm \sqrt{Z_o^2-4}}{2} \qquad (2.21)$$

and

$$t_{o,i} = \frac{\overline{Z}_o \pm \sqrt{\overline{Z}_o^2-4}}{2} \qquad (2.22)$$

Evaluating the integrals of Eqs. (2.20) leads to

$$\varphi_1^*(\zeta) = \frac{P_k^*(Z_o)}{2\pi(\alpha+1)} \left[\ell n \frac{r_o-\zeta}{r_o} - \alpha\, \ell n \frac{t_o-\zeta}{t_o}\right]$$

$$+ \frac{\overline{P_k^*(Z_o)}}{2\pi(\alpha+1)} \left[\frac{\zeta^2-Z_o\zeta+1}{\zeta^2-\overline{Z}_o\zeta+1} + \frac{(t_i^2-Z_o t_i+1)\zeta}{t_i(t_o-t_i)(\zeta-t_i)} - 1\right]$$

$$\psi_1^*(\zeta) = \frac{P_k^*(Z_o)}{2\pi(\alpha+1)} \left[\frac{\zeta^2-\overline{Z}_o\zeta+1}{\zeta^2-Z_o\zeta+1} + \frac{r_i^2-\overline{Z}_o r_i+1}{r_i(r_o-r_i)(\zeta-r_i)}\right.$$

$$\left. + \frac{\zeta(\zeta^2+1)}{1-\zeta^2} \left(\frac{1}{\zeta-r_o} - \frac{\zeta}{\zeta-t_o}\right) - 1\right]$$

$$+\frac{\overline{P_k^*(Z_o)}}{2\pi(\alpha+1)}\left[\ell n\,\frac{t_o-\zeta}{t_o}-\alpha\,\ell n\,\frac{r_o-\zeta}{r_o}\right.$$

$$\left.+\frac{\zeta(\zeta^2+1)}{1-\zeta^2}\left\{\frac{(Z_o-\bar{Z}_o)(2\zeta^2-Z_o\zeta)}{(\zeta^2-\bar{Z}_o\zeta+1)^2}-\frac{t_i^2-Z_o t_i+1}{(t_o-t_i)(\zeta-t_i)^2}\right\}\right] \tag{2.23}$$

provided that $\zeta \neq t_i$. If $\zeta = t_i$, i.e. $Z = \bar{Z}_o$, one obtains

$$\varphi_1^*(t_i)=\frac{P_k^*(Z_o)}{2\pi(\alpha+1)}\left[\ell n\,\frac{r_o-t_i}{r_o}-\alpha\,\ell n\,\frac{t_o-t_i}{t_o}\right]$$

$$+\frac{\overline{P_k^*(Z_o)}}{2\pi(\alpha+1)}\left[\frac{t_i^2-2t_i t_o+Z_o t_o-1}{(t_i-t_o)^2}-\frac{Z_o t_o-1}{t_o^2}\right] \tag{2.24}$$

$$\psi_1^*(t_i)=\frac{P_k^*(Z_o)}{2\pi(\alpha+1)}\left[\frac{t_i^2-\bar{Z}_o t_i+1}{t_i^2-Z_o t_i+1}+\frac{r_i^2-\bar{Z}_o r_i+1}{r_i(r_o-r_i)(t_i-r_i)}\right.$$

$$\left.+\frac{t_i(t_i^2+1)}{1-t_i^2}\left(\frac{1}{t_i-r_o}-\frac{\alpha}{t_i-t_o}\right)-1\right]$$

$$+\frac{\overline{P_k^*(Z_o)}}{2\pi(\alpha+1)}\left[\ell n\,\frac{t_o-t_i}{t_o}-\alpha\,\ell n\,\frac{r_o-t_i}{r_o}\right.$$

$$\left.+\frac{t_i(t_i^2+1)}{1-t_i^2}\,\frac{2(t_o^2-Z_o t_o+1)}{(t_i-t_o)^3}\right]$$

Since φ_1^* and ψ_1^* are now known, φ^* and ψ^* are also known via Eqs. (2.11) and the Boundary-Integral procedure outlined earlier can be applied.

3. THEORETICAL RESULTS

The Boundary-Integral method developed in Section 2 is now applied to example problems involving mixed-mode loading conditions. The results will be compared to some experimental results in Section 6.

3.1 Definition of Example Problems

Consider the problem of Figure 3.1, i.e. a rectangular region, containing a centrally-located sharp crack of half-length a = 6.40 mm and subjected to uniaxial tension of 1 MPa. Plane stress is assumed and $\nu = .33$, $E = 70 \times 10^3$ MPa. The following 36 cases are treated: W = 7.62 cm, 4.37 cm, 3.05 cm, 2.34 cm, 1.90 cm, 1.60 cm; and $\theta = 0^\circ$, 15°, 30°, 45°, 60°, 75°. For all cases, the displacements in the x and y directions of the 6 field points shown in Figure 3.2, are computed. The results are presented in Tables 3.1 - 3.6 where all displacements are given in microns.

For implementation of Eqs. (2.4) and (2.5), the boundary has been divided into N = 60 divisions, 10 divisions on each of the loaded sides of length $\Delta S_\ell = W/10$ and 20 divisions on each of the unloaded sides of length $\Delta S_\ell = 3W/20$. The solution of Eqs. (2.4) was obtained by Gaussian elimination (Crout algorithm) with equilibration and partial pivoting. Since a crack of half-length a = 2 was assumed in Section 2, the problem was first scaled accordingly and the solutions were subsequently scaled back.

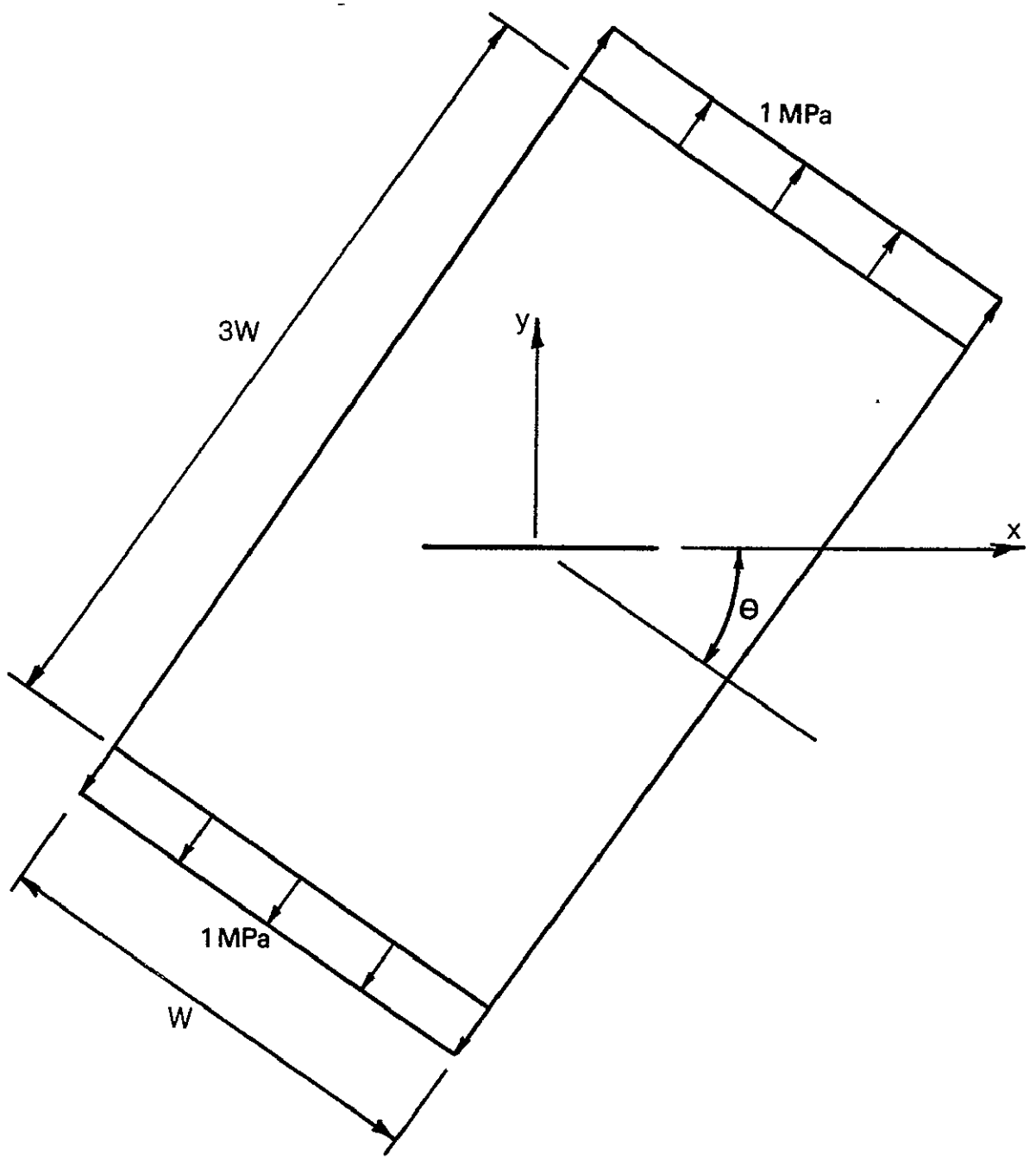

Figure 3.1. Geometry of Example Problems

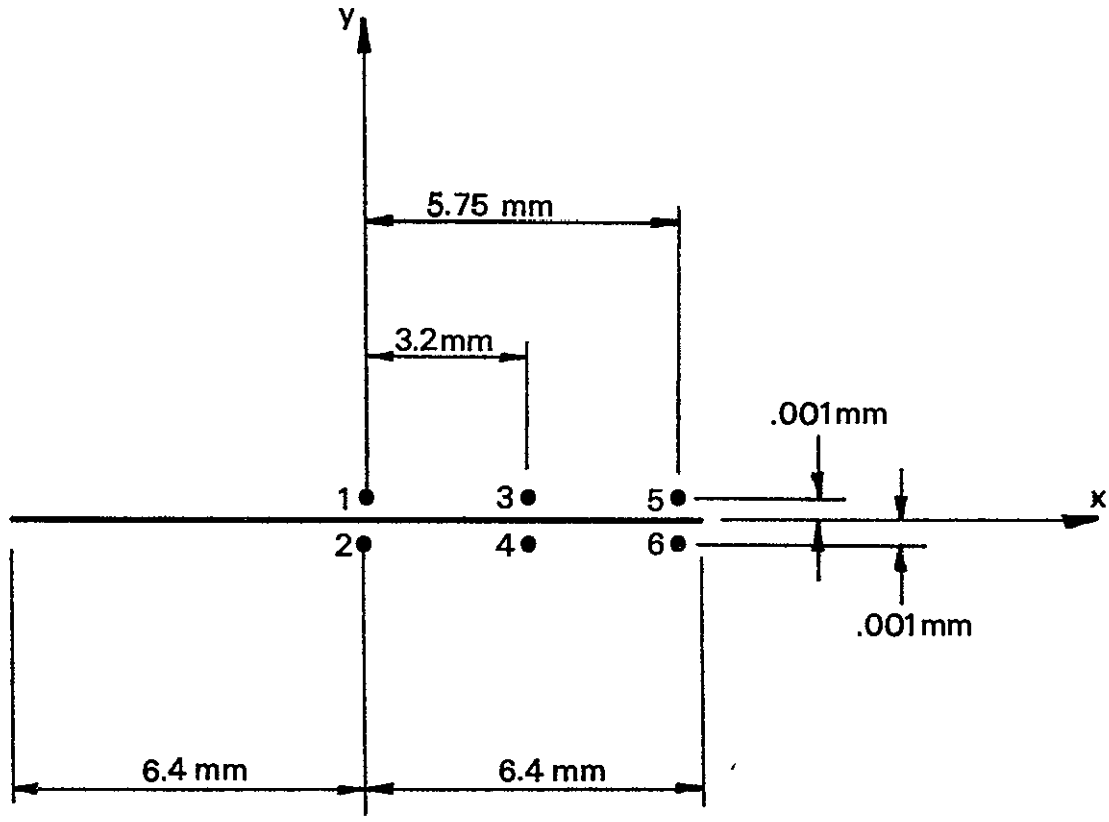

Figure 3.2. Location of Field Points.

3.2 Results

TABLE 3.1

Displacement (microns) for W = 7.62 cm

Field Point	1		2		3		4		5		6	
θ	u_x	u_y	u_x	u_y	u_x	u_y	u_x	u_y	u_x	u_y	u_x	u_y
0°	.000	.186	.000	-.186	-.035	.155	-.035	-.155	-.064	.040	-.064	-.040
15°	.046	.174	-.046	-.174	.011	.169	-.071	-.119	-.027	.082	-.080	.009
30°	.080	.140	-.080	-.140	.057	.159	-.085	-.072	.021	.105	-.072	.052
45°	.093	.093	-.093	-.093	.089	.127	-.075	-.026	.067	.103	-.041	.079
60°	.080	.047	-.080	-.047	.100	.081	-.043	.007	.098	.078	.004	.081
75°	.047	.012	-.047	-.012	.086	.033	.003	.018	.107	.034	.052	.058

TABLE 3.2

Displacement (microns) for W = 4.37 cm

Field Point	1		2		3		4		5		6	
θ	u_x	u_y	u_x	u_y	u_x	u_y	u_x	u_y	u_x	u_y	u_x	u_y
0°	.000	.193	.000	-.193	-.037	.160	-.037	-.160	-.066	.041	-.066	-.041
15°	.046	.180	-.046	-.180	.010	.176	-.072	-.123	-.029	.085	-.083	.010
30°	.081	.146	-.081	-.146	.056	.166	-.087	-.075	.020	.109	-.076	.056
45°	.094	.098	-.094	-.098	.090	.134	-.078	-.026	.067	.109	-.046	.084
60°	.083	.049	-.083	-.049	.101	.086	-.046	.008	.099	.083	.000	.086
75°	.048	.013	-.048	-.013	.087	.036	.001	.019	.108	.037	.050	.061

TABLE 3.3

Displacement (microns) for W = 3.05 cm

Field Point	1		2		3		4		5		6	
θ	u_x	u_y	u_x	u_y	u_x	u_y	u_x	u_y	u_x	u_y	u_x	u_y
0^o	.000	.204	.000	-.204	-.039	.170	-.039	-.170	-.071	.044	-.071	-.044
15^o	.046	.192	-.046	-.192	.008	.187	-.075	-.131	-.032	.090	-.089	.011
30^o	.082	.156	-.082	-.156	.055	.178	-.091	-.079	.017	.117	-.083	.061
45^o	.097	.106	-.097	-.106	.090	.144	-.083	-.028	.066	.118	-.053	.092
60^o	.086	.054	-.086	-.054	.103	.094	-.050	.010	.101	.091	-.005	.094
75^o	.050	.014	-.050	-.014	.089	.039	-.001	.021	.110	.042	.047	.066

TABLE 3.4

Displacement (microns) for W = 2.34 cm

Field Point	1		2		3		4		5		6	
θ	u_x	u_y	u_x	u_y	u_x	u_y	u_x	u_y	u_x	u_y	u_x	u_y
0^o	.000	.223	.000	-.223	-.043	.186	-.043	-.186	-.077	.048	-.077	-.048
15^o	.047	.210	-.047	-.210	.005	.204	-.079	-.144	-.038	.100	-.097	.014
30^o	.083	.172	-.083	-.172	.053	.195	-.096	-.087	.014	.130	-.093	.070
45^o	.100	.117	-.100	-.117	.091	.159	-.089	-.030	.065	.131	-.063	.103
60^o	.090	.060	-.090	-.060	.105	.104	-.056	.011	.102	.101	-.013	.104
75^o	.053	.015	-.053	-.015	.091	.044	-.004	.024	.112	.048	.044	.072

TABLE 3.5

Displacement (microns) for W = 1.90 cm

Field Point	1		2		3		4		5		6	
θ	u_x	u_y	u_x	u_y	u_x	u_y	u_x	u_y	u_x	u_y	u_x	u_y
0^o	.000	.253	.000	-.253	-.047	.212	-.047	-.212	-.087	.055	-.087	-.055
15^o	.047	.238	-.047	-.238	.000	.233	-.085	-.164	-.045	.118	-.112	.020
30^o	.084	.195	-.084	-.195	.050	.219	-.102	-.100	.009	.148	-.107	.082
45^o	.103	.134	-.103	-.134	.090	.178	-.096	-.034	.063	.148	-.076	.118
60^o	.094	.068	-.094	-.068	.107	.117	-.062	.013	.103	.114	-.022	.117
75^o	.056	.017	-.056	-.017	.093	.050	-.008	.027	.114	.055	.039	.079

TABLE 3.6

Displacement (microns) for W = 1.60 cm

Field Point	1		2		3		4		5		6	
θ	u_x	u_y	u_x	u_y	u_x	u_y	u_x	u_y	u_x	u_y	u_x	u_y
0^o	.000	.300	.000	-.300	-.051	.254	-.051	-.254	-.096	.067	-.096	-.067
15^o	.050	.287	-.050	-.287	-.003	.291	-.097	-.192	-.047	.172	-.145	.048
30^o	.084	.231	-.084	-.231	.045	.255	-.110	-.123	.001	.177	-.128	.099
45^o	.106	.156	-.106	-.156	.089	.203	-.104	-.041	.061	.169	-.093	.137
60^o	.098	.079	-.098	-.079	.109	.132	-.069	.014	.103	.128	-.033	.131
75^o	.059	.020	-.059	-.020	.096	.057	-.012	.031	.116	.062	.035	.086

4. EXPERIMENTAL TECHNIQUES

This section describes the application of a novel displacement measuring technique - the interferometric displacement gage (IDG) - to the measurement of biaxial displacements across slots subjected to mixed-mode loading. The basics of the IDG are first presented followed by a description of a fringe-counting instrument that was developed for these measurements. The material properties and geometries of the specimens are then given. Experimental results from the more than 200 tests are presented in tabular and graphical form in the next section.

4.1 The Interferometric Displacement Gage (IDG)

The principles of the IDG have been described in detail in Reference (1); only a basic review of the technique is given here. Extension of the uniaxial IDG to biaxial displacement measurement poses special problems that are also discussed.

4.1.1 Basics of the IDG

Shallow reflective indentations are pressed into the polished surface of the specimen on either side of a crack or slot as shown in Figure 4.1. When coherent light impinges upon the indentations, it is diffracted back at an angle (α_o) with respect to the incident beam shown schematically in Figure 4.1. Since the indentations are placed close together, the respective diffracted beams overlap, resulting in interference fringe patterns on either side of the incident laser beam.

In observing the fringe pattern from a fixed position at the angle α_o, fringe movement occurs as the distance (d) between the indentations changes. Application of a tensile load, causing the distance between the indentations to increase, results in positive fringe motion towards the

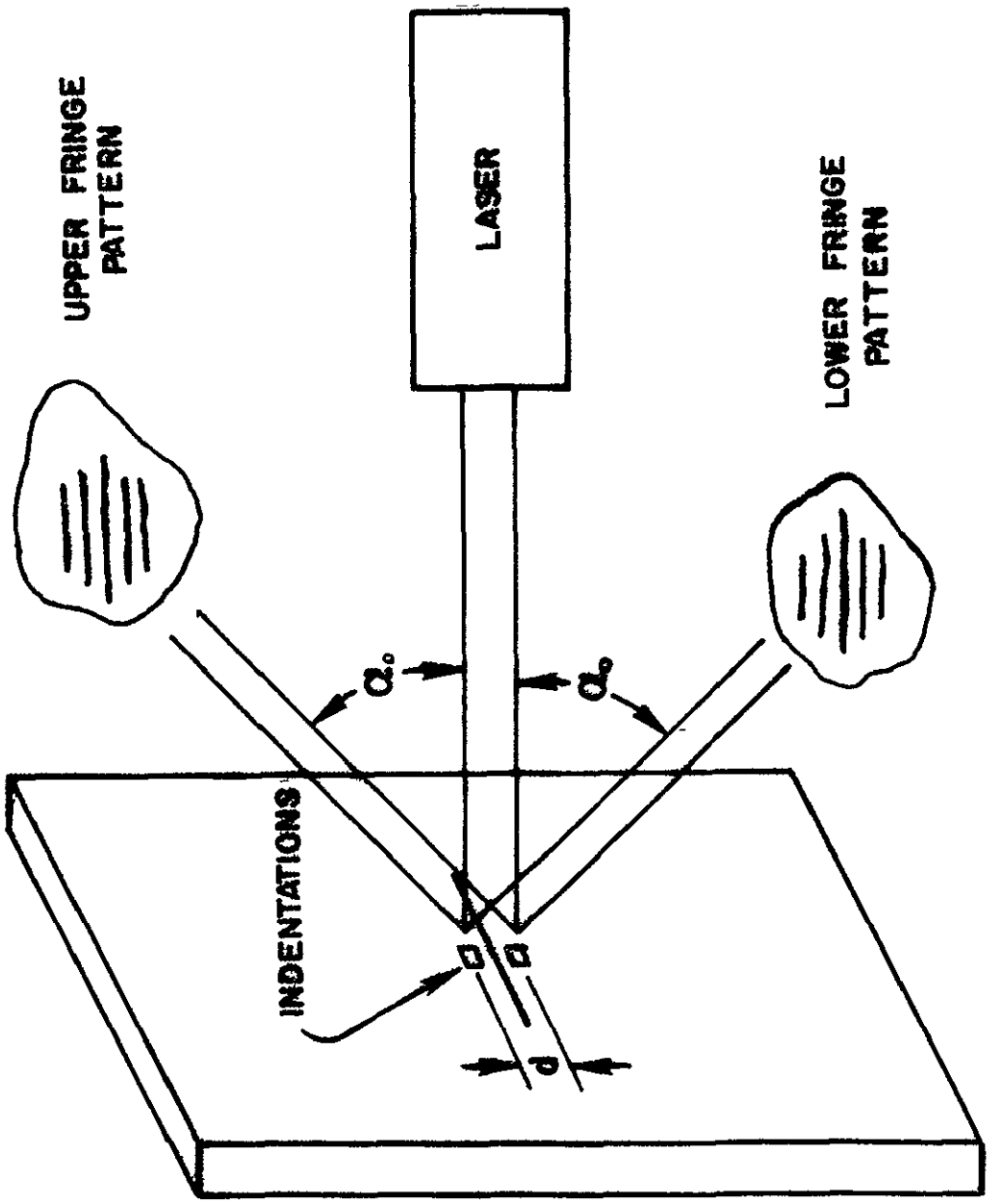

Figure 4.1 Schematic of the IDG.

incident beam. Conversely, the removal of the tensile load results in negative fringe motion away from the incident beam.

The relationship between the indentation spacing and the fringe order shown schematically in Figure 4.1 is (1):

$$d \sin \alpha_o = m\lambda \tag{4.1}$$

Here m is the fringe order, d the spacing between indentations, λ the wave length of the incident beam, and α_o the angle between the incident and reflected beams, thus defining the zeroth fringe order.

The relationship between the change in indentation spacing (δd) and the change in fringe order at the fixed observation point (δm) is given by

$$\delta d = \frac{\delta m \lambda}{\sin \alpha_o} \tag{4.2}$$

It is this relation that serves as the basis of the IDG.

Fringe motion can be caused by rigid body motion as well as relative displacement. When the specimen moves parallel to its surface and along a line between the indentations (i.e., vertically in Figure 4.1), one fringe pattern moves toward the incident beam, and one moves away. Therefore, averaging the fringe motions eliminates the rigid body motion, and one should calculate the displacement from:

$$\delta d = \frac{\lambda}{\sin \alpha_o} \quad \frac{\delta m_1 + \delta m_2}{2} \tag{4.3}$$

This component of rigid-body motion is present in every ordinary system for loading specimens, so that it is very important that it be averaged out. Other rigid-body motions (e.g., one perpendicular to the specimen surface) are not averaged out and can lead to errors. In a carefully

aligned testing machine these components of rigid-body motion can be made small, eliminating the need for corrections.

Using typical values of $\lambda = 0.6328$ microns (He-Ne laser) and $\alpha_o = 42^o$, the calibration constant $\lambda/\sin\alpha_o$ is 0.95 microns. In other words, when one complete fringe shift has been observed, the corresponding displacement is about one micron. An electro-optical recording system that simply counts the fringes of one pattern as they pass will have a resolution of one micron. A recording system that counts both patterns and increments the output voltage whenever either pattern moves one fringe will have a resolution of one-half micron.

The "gage" consists of the two reflecting indentations. These are applied with a Vicker's hardness tester which, with its diamond indenter, permits the accurate location and application of high quality pyramidal indentations. These indentations are typically 25 microns long on each side and can be placed as close as 25 microns to the edge of a crack. Details of the application of indentations to the biaxial specimens are given in sections 4.3.3 and 4.3.4.

4.1.2 The IDG for Biaxial Displacement Measurements

The IDG can be readily adapted to biaxial measurement, but it is not simply a matter of adding a third indentation to form a second gage. It is useful to examine the fringe patterns generated by various configurations of indentations.

Figure 4.2 is a photomicrograph of a pair of indentations and its corresponding fringe pattern. The orientation of the indentations is the same as in Figure 4.1; the fringe pattern shown is the lower one. There are four fringe patterns generated, one from each parallel side of the indentations. The fringes of each pattern are parallel to the ones shown

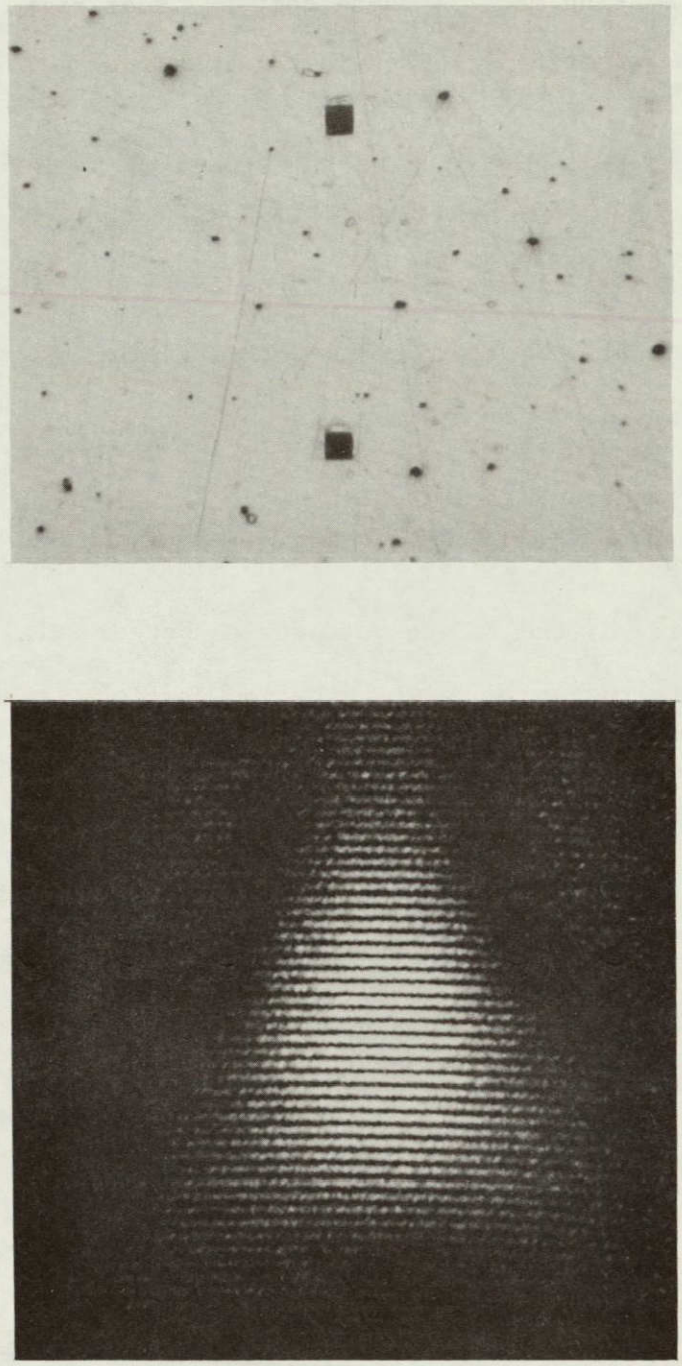

Figure 4.2 Photomicrograph of a set of two indentations and a resulting fringe pattern. The indentations are 25 microns on a side and 300 microns apart. The fringe pattern was photographed 60 cm. from the specimen.

in the figure. The indentations are 25 microns square and 300 microns apart. The triangular shape of the overall pattern results from diffraction from a triangular side of the pyramidal indentation. It is obvious from looking at the fringe pattern that a photodetector with a long, narrow slit aperture will give a better signal-to-noise ratio than one with a circular aperture. The photodetectors used have an optical system equivalent to a long, thin aperture.

Indentations located at 45 degree angles and the resulting pattern are shown in Figure 4.3. Since the sides of the indentations are parallel but displaced, the fringe pattern is skewed. The angle of skewness is related to the angle between the indentations in a fairly complicated way (2). It turns out that when the indentations are located at large angles, the skewness of the fringes is relatively insensitive to the indentation angle; measurement of the fringe pattern skewness is not a good way to measure displacement. However, it would be possible to locate four photodetectors with small apertures at the four fringe patterns and simply count the fringes as they pass - ignoring the small change in skewness. This is impractical to do for these biaxial specimens with a low intensity laser because:

a) the slots in the specimens are roughly 400 microns wide, so the indentations in Figure 4.3 are not far enough apart,

b) putting the indentations further apart reduces the fringe spacing,

c) the aperture of the photodetector then has to be smaller, requiring a more expensive sensor.

This problem could be alleviated with a more powerful laser. There are limits to the indentation spacing because the fringes eventually become so small that they are on the order of the "speckles" in the diffracted pattern.

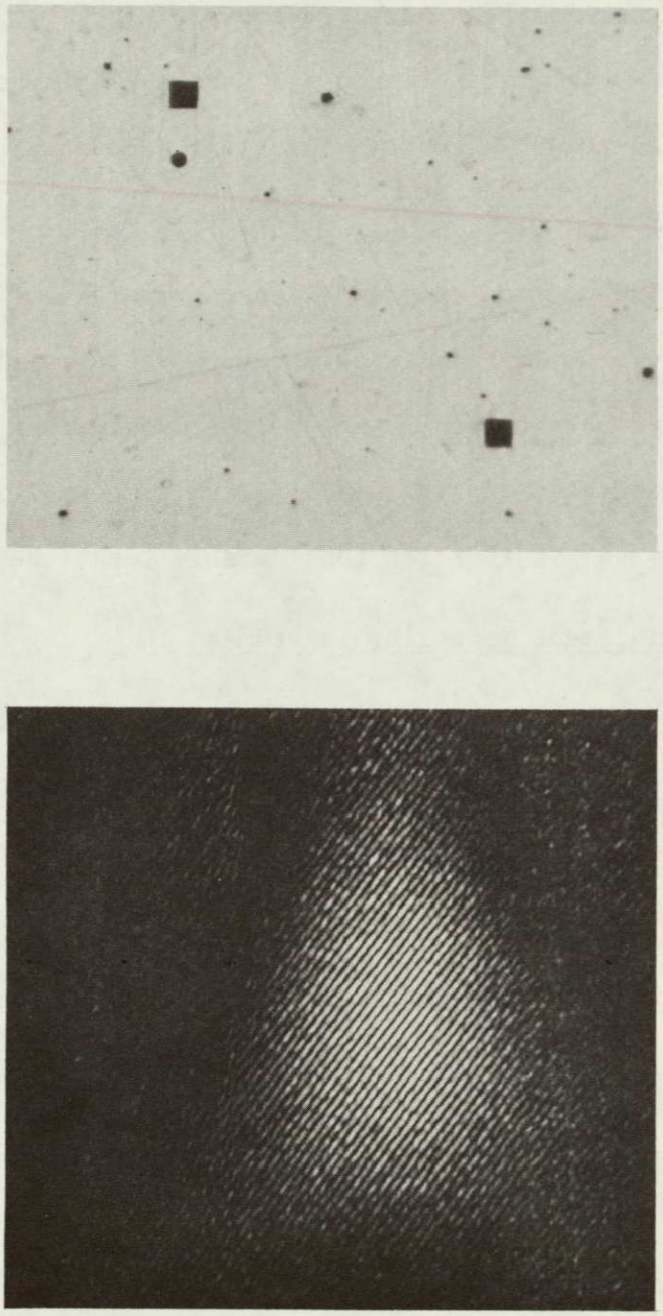

Figure 4.3 Photomicrograph of two indentations at a 45° angle and a fringe pattern. Magnification same as Figure 4.2.

A direct approach to biaxial measurement is shown in Figure 4.4. The fringe pattern is "checkered" because of the overlap of two uniaxial fringe patterns. However, one can use a narrow-slitted aperture to still get a good signal-to-noise ratio. This is the configuration used for these measurements.

The indentation configuration of Figure 4.4 is fine for biaxial strains, but not biaxial displacements across a slot. It is therefore necessary to attach small tabs to the specimen in an arrangement schematically illustrated in Figure 4.5. Details of how this is done are given in Section 4.3.4; it required considerable technique development.

4.2 Displacement Measuring Instrument

An electro-optical instrument was developed to count the fringe motion from two patterns and produce a voltage output proportional to displacement. The simple analog counting device and the specifications of the instrument are presented in this section.

4.2.1 Photodetectors and Mounting Stage

The photodetectors are Type 2N5777 phototransistors. Although their aperture is only ~ 200 microns in diameter, when placed approximately 40 cm from a set of indentations 400 microns apart that are illuminated with a 5 milliwatt laser, the output voltage changes by approximately 0.1 volt as the fringe pattern moves. To increase this signal change as well as to generate the equivalent of a slit aperture, a cylindrical lens is placed in front of the phototransistor. Figure 4.6 is a schematic of the optical arrangement. The cylindrical lens is oriented with its axis perpendicular to the fringes; this causes the fringes to be compressed along their length, but their spacing remains unchanged at the detector. The detector

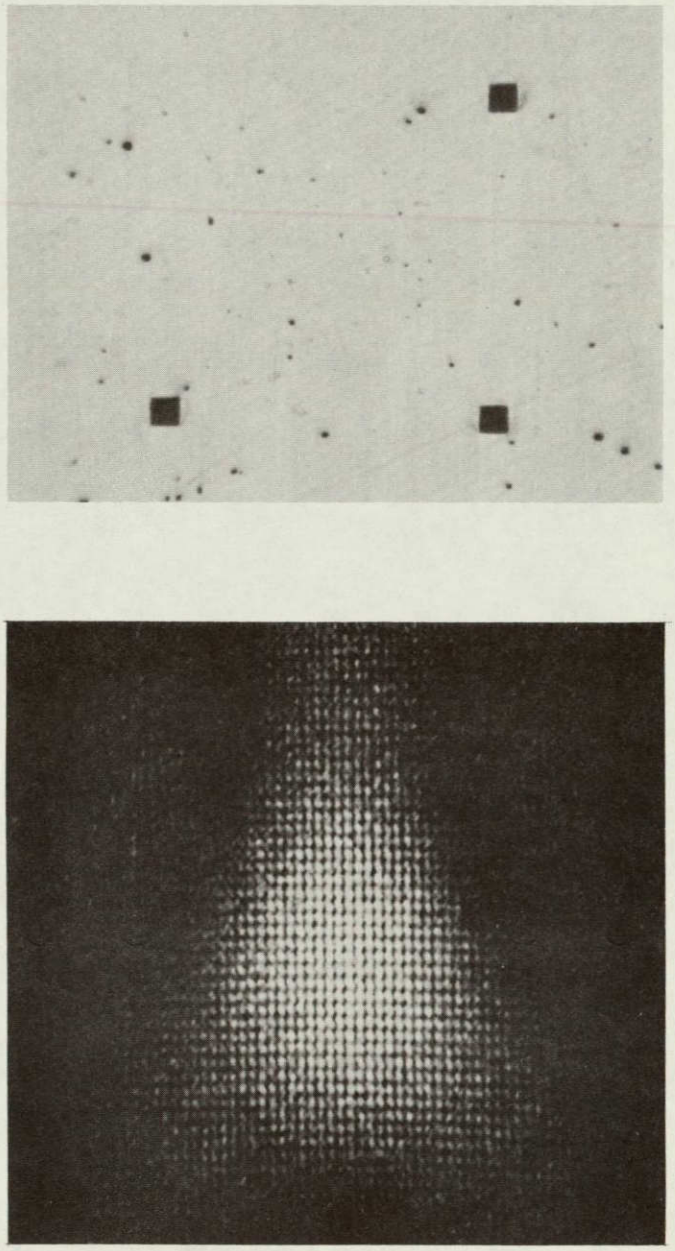

Figure 4.4 Photomicrograph of three indentations and a fringe pattern. Magnification same as Figure 4.2.

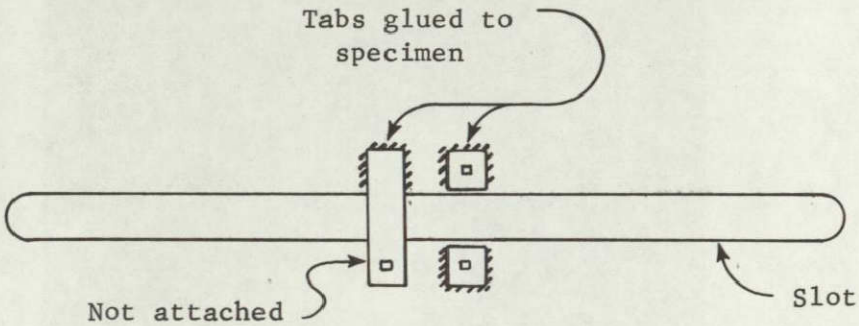

Figure 4.5 Schematic of tab arrangement for biaxial displacement measurement.

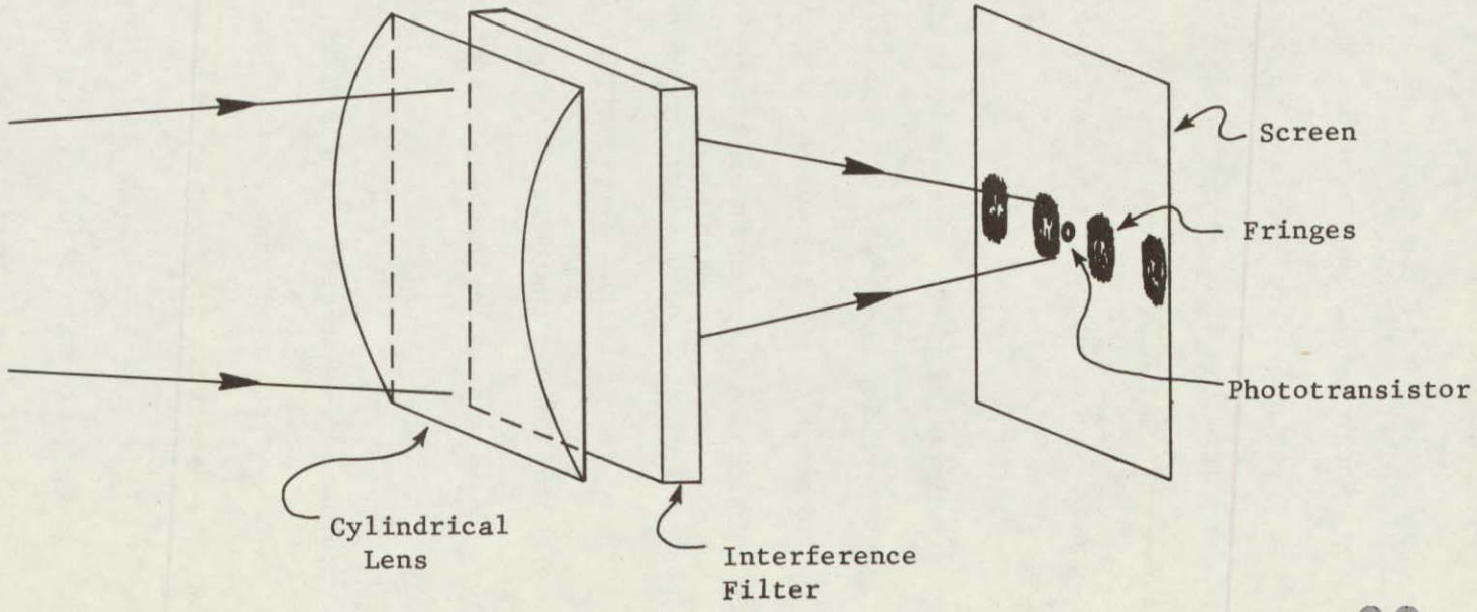

Figure 4.6 Schematic of the optical arrangement in front of the phototransistor.

thus receives a brighter fringe pattern with a resulting higher signal-to-noise ratio, and it "sees" a slit at the cylindrical lens. The focal length of the lens is 44 mm. The detector is not placed at the focal point because the pattern would then be a series of small dots and alignment would be more critical. Instead, the detector is positioned at approximately 37 mm from the lens so that the fringes are roughly 2 mm wide at the detector. An interference filter is inserted behind the lens to reduce background light. A photograph of the photodetector assembly is in Figure 4.7.

This arrangement using phototransistors is the final version of the system. An earlier version used type UDT-600 photodiode-amplifiers manufactured by United Detector Technology, Inc., Santa Monica, CA. The earlier version was chosen because of previous experience with it at MSU and was used for most of the tests. The photodiode has an aperture of 1 mm which was then covered with a slit-aperture 0.1 mm wide. The operation of the two photodetector systems is basically the same; however, the phototransistor one is considerably cheaper and requires a simpler power supply (+15 volts versus $\pm$ 15 volts for the diode).

Four photodetectors are required for biaxial displacement measurement and they must each be capable of easy positioning relative to the fringe patterns. The four detectors are mounted on microscope translation stages which are attached to a four-armed frame. The frame can rotate about the axis of the incident laser beam to permit displacement measurements at various angles. The frame is typically located 30 cm from the specimen. A photograph of the mounting stage is in Figure 4.8; the entire assembly is pictured in front of an Instron testing machine in Figure 4.9.

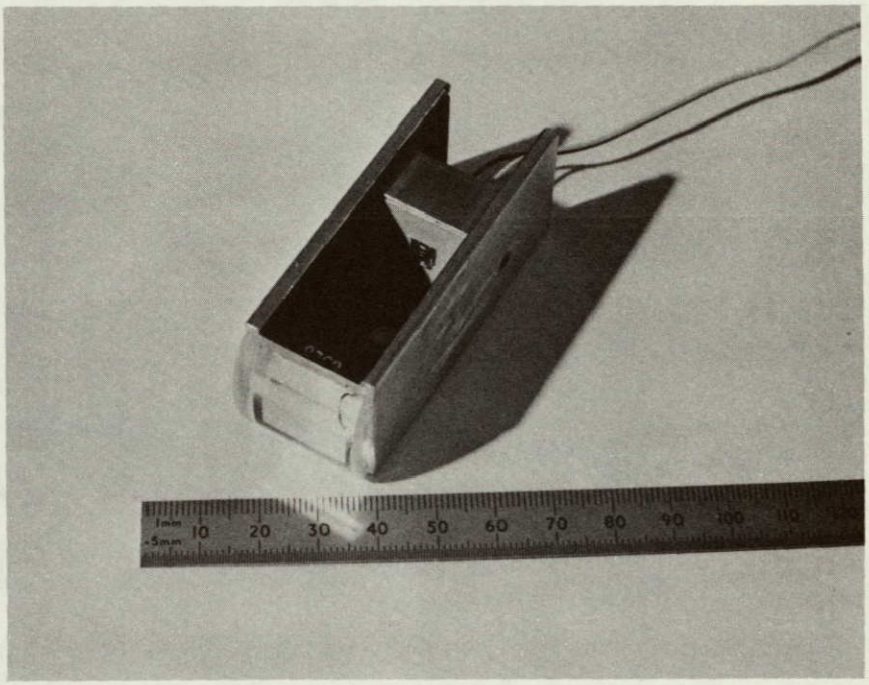

Figure 4.7 Photograph of the photodetector assembly.

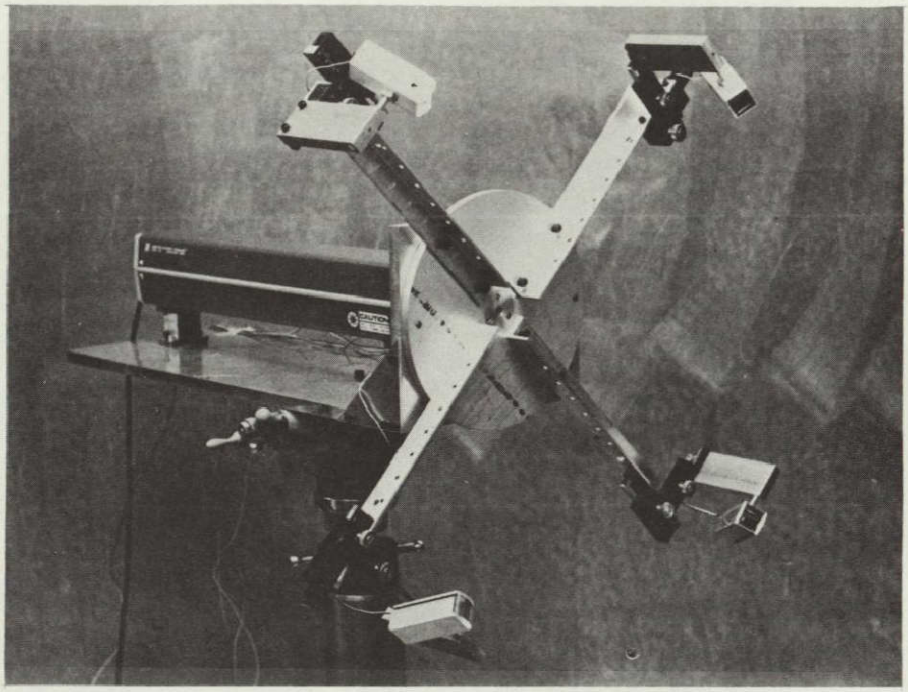

Figure 4.8 The mounting stage for the four photodetectors.

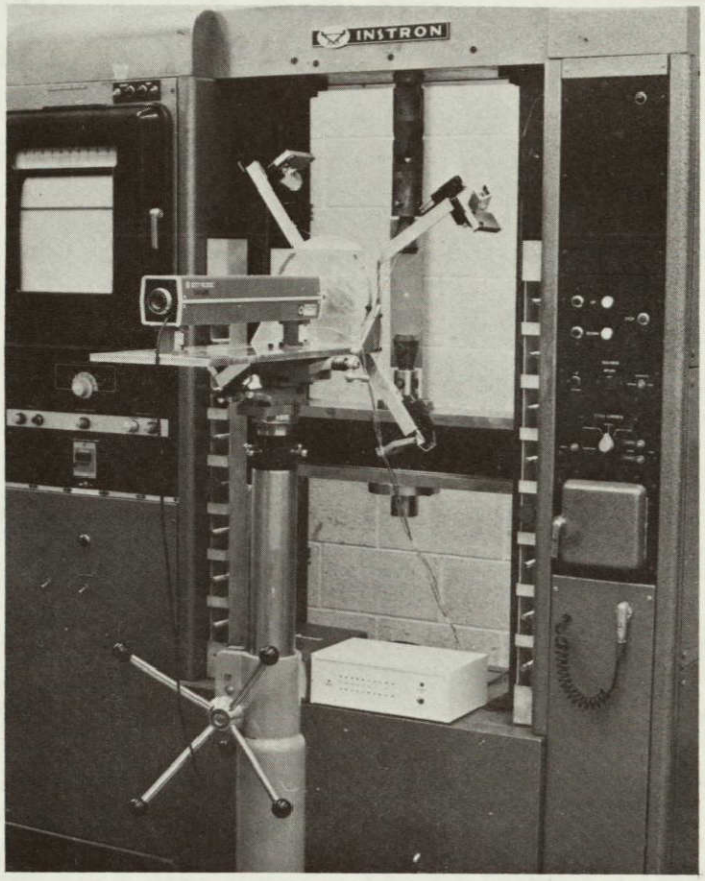

Figure 4.9 The biaxial displacement measuring instrument in position in front of the testing machine.

4.2.2 Fringe Counting Circuit

A block diagram of the circuit is given in Figure 4.10. The output from the phototransistor goes through a low-pass filter (10 hz) to a low-gain amplifier with variable gain (0.1X-100X) and zero positioning. These adjustments are necessary because the fringe patterns vary in intensity for different pairs of indentations. This variation is not extreme, but the voltage that is presented to the "one-shot" must be within certain limits. A voltage output proportional to the pattern intensity is provided so that the gain and offset can be adjusted while monitoring with an external voltmeter. The intensity voltage goes to a limiting diode which prohibits the voltage behind it from exceeding 5 volts. This limited voltage then triggers a one-shot monostable multivibrator that outputs a pulse every time the incoming voltage is increasing and exceeds a certain level ($\sim$ 1 volt). In other words, one pulse is generated every time a fringe passes the phototransistor. This pulse is fed into a summing circuit which increments once for each pulse received. The "summer" counts pulses from both channels and thus effects the averaging of the fringe motions. The output from the summer goes to an LED display which gives the fringe count in digital form and to a digital-to-analog converter which gives an output voltage proportional to displacement. This voltage is of course incremental, so a typical load-displacement curve looks like Figure 4.11. Each voltage increment parallel to the displacement axis corresponds to a displacement of

$$\frac{1}{2} \frac{\lambda}{\sin \alpha_o}$$

because of the averaging. It is very easy to pre-or post-calibrate the displacement scale.

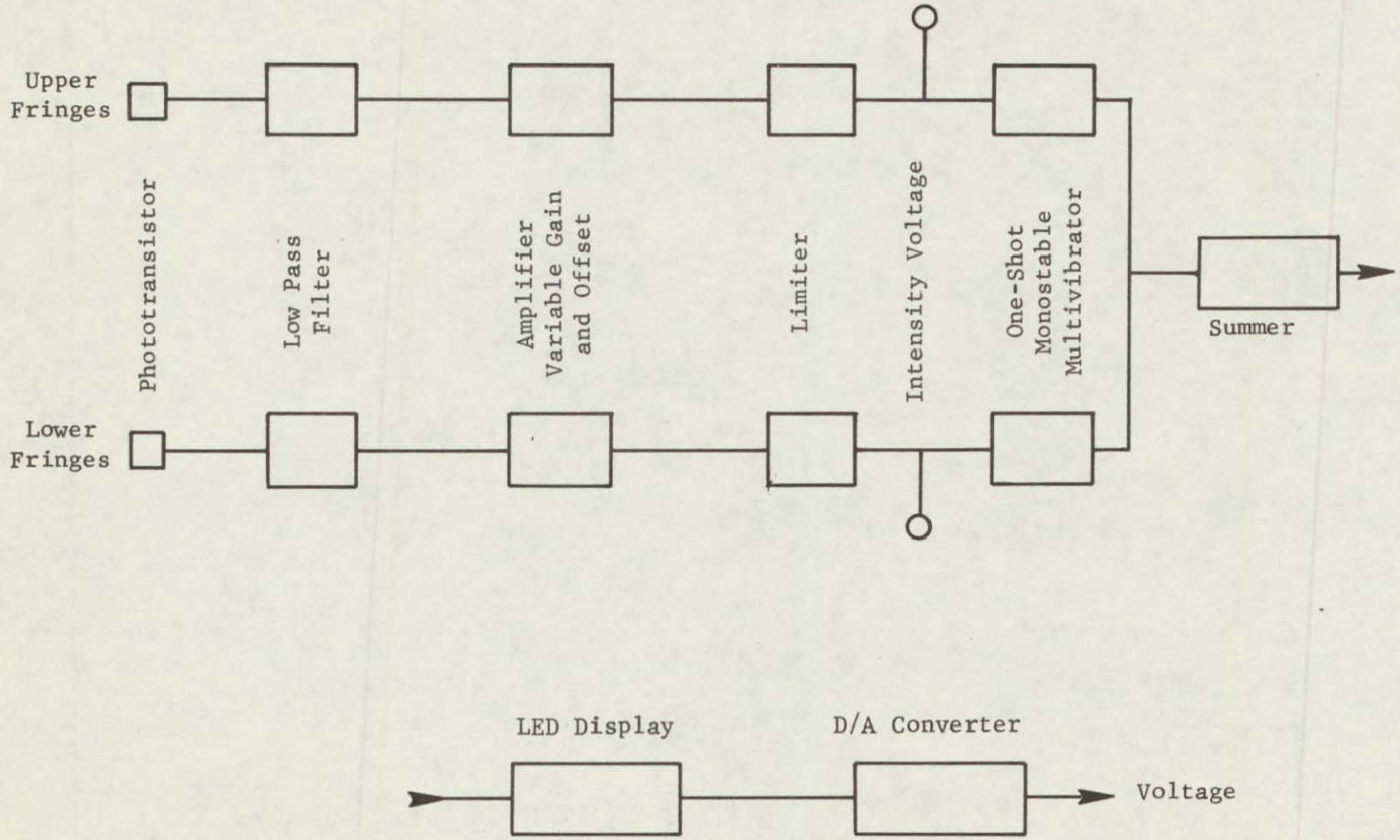

Figure 4.10 Block diagram of the fringe counting circuit.

Figure 4.11 A typical load-displacement curve.

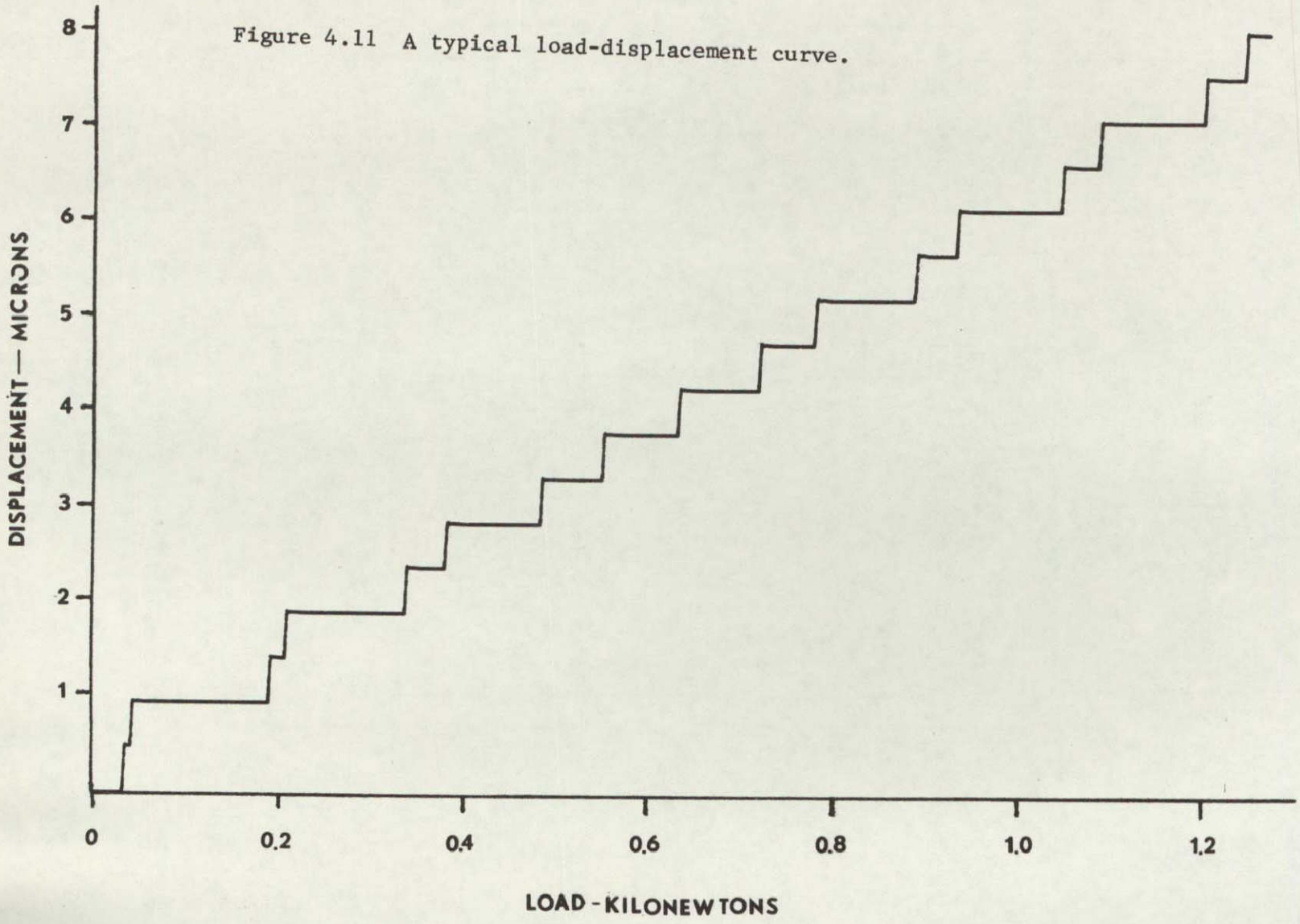

A detailed circuit diagram of the complete biaxial counter is presented in Figures 4.12 and 4.13. Photographs of the front and back and the circuit board of the counter are in Figures 4.14 and 4.15. The location of the electronic components is shown in Figure 4.16.

4.2.3 Operating Procedures

The following procedures should be used in setting up the fringe counter for measurements:

1. Align the incident laser beam. The laser beam is narrow (~ 1 mm diameter) with a bell-shaped intensity distribution. It must be aligned so that the indentations are illuminated at the beginning of loading and throughout the experiment. The fringe counter can tolerate some variation in intensity, but not extreme changes. If a lot of rigid-body motion occurs during the experiment, a cylindrical lens can be used to spread the laser beam in the direction of motion (3). The specimen reflects a portion of the incident beam which can be observed on the laser head and used as a guide in adjusting the laser position to insure perpendicularity of the incident beam.
2. Align the photodetectors. They must be positioned so that the fringe pattern falls on the cylindrical lens. Typically the total fringe pattern is about the size of the lens. The detectors must then be oriented angularly so that the pattern falls on the phototransistor. A sliding cover on the photodetector case and a white background around the transistor make this task easier. If necessary, the phototransistor can be moved along the optical axis in the case to adjust the size of the fringes at the transistor. The final arrangement should be a row of fringes approximately 2.5 mm high centered about the phototransistor.

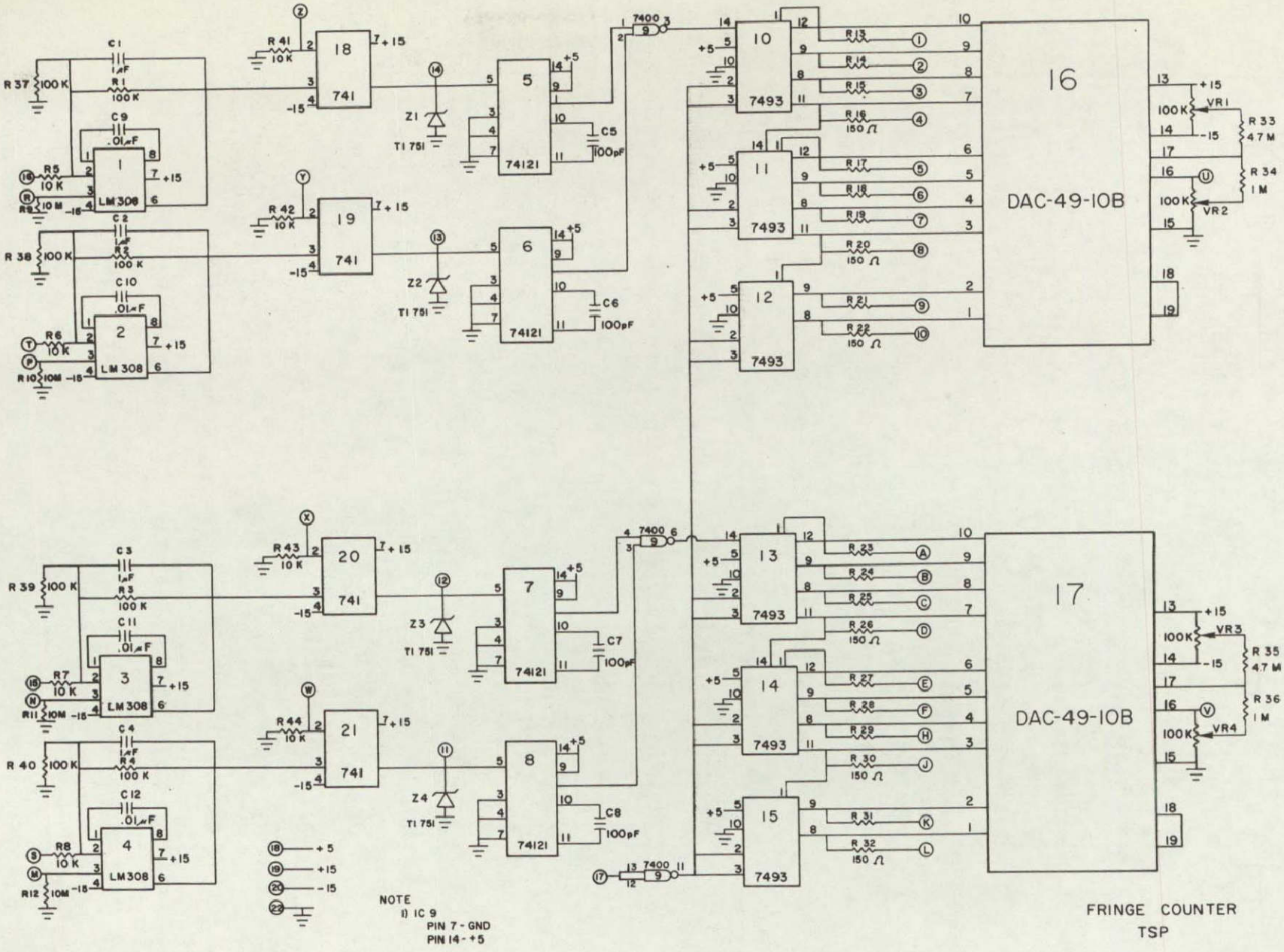

Figure 4.12 Circuit diagram of the biaxial fringe counter - Part 1.

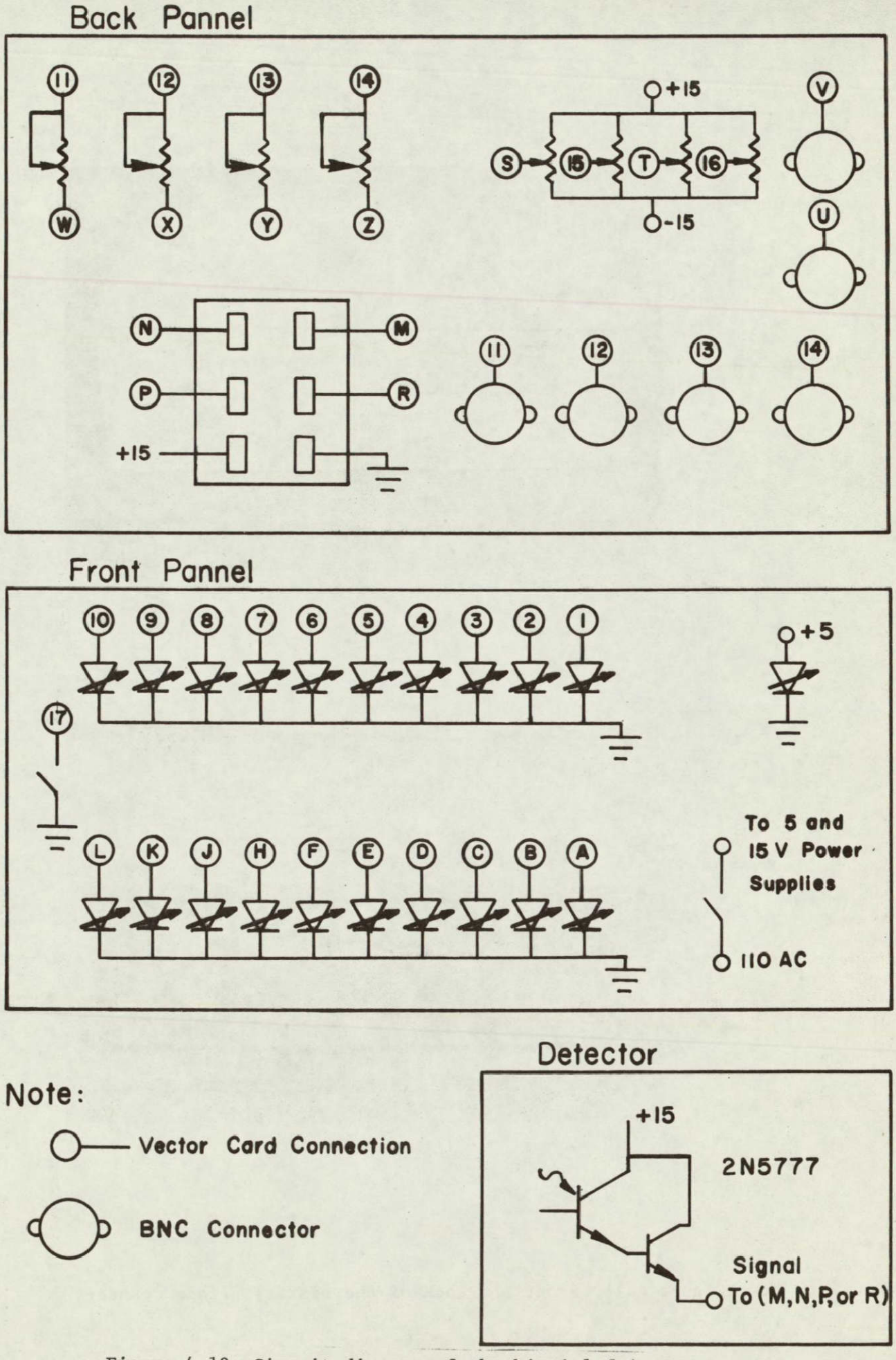

Figure 4.13 Circuit diagram of the biaxial fringe counter - Part 2.

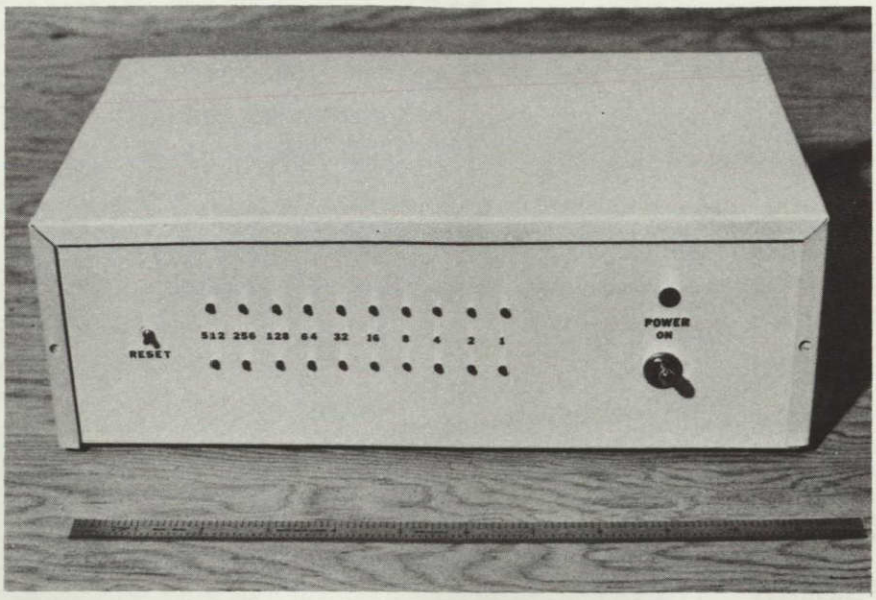

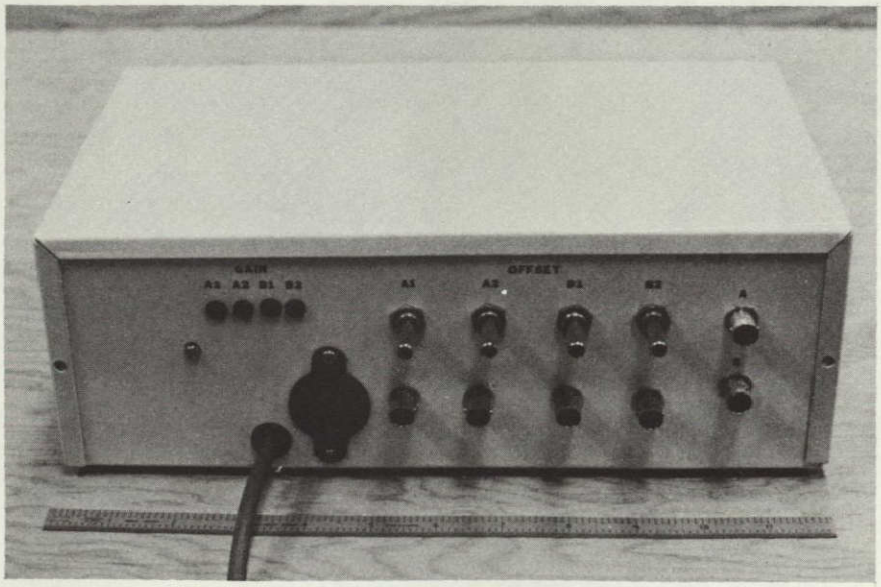

Figure 4.14 Front and back of the biaxial fringe counter.

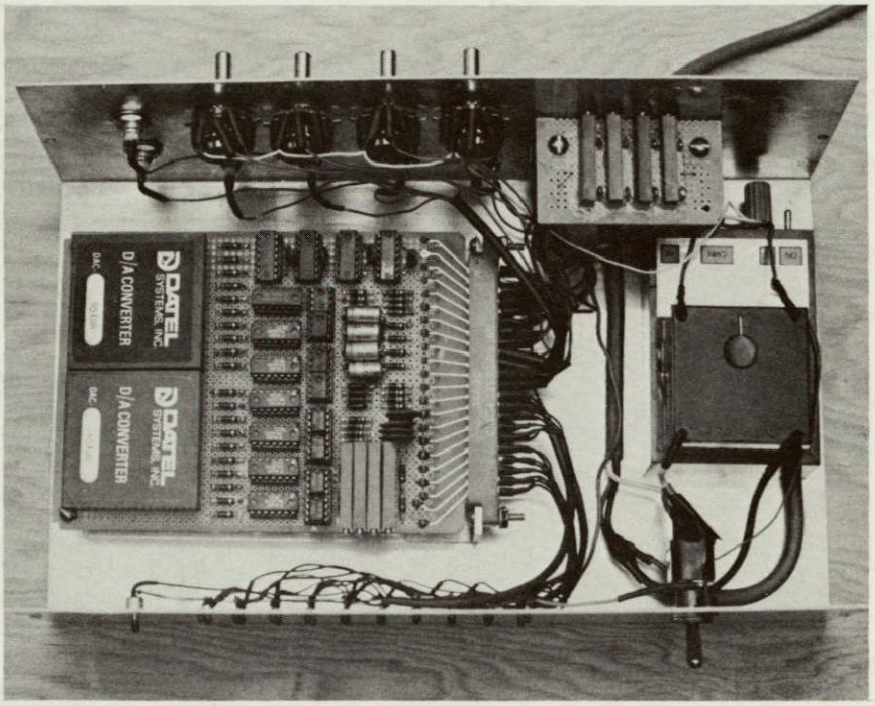

Figure 4.15 Interior of the biaxial fringe counter.

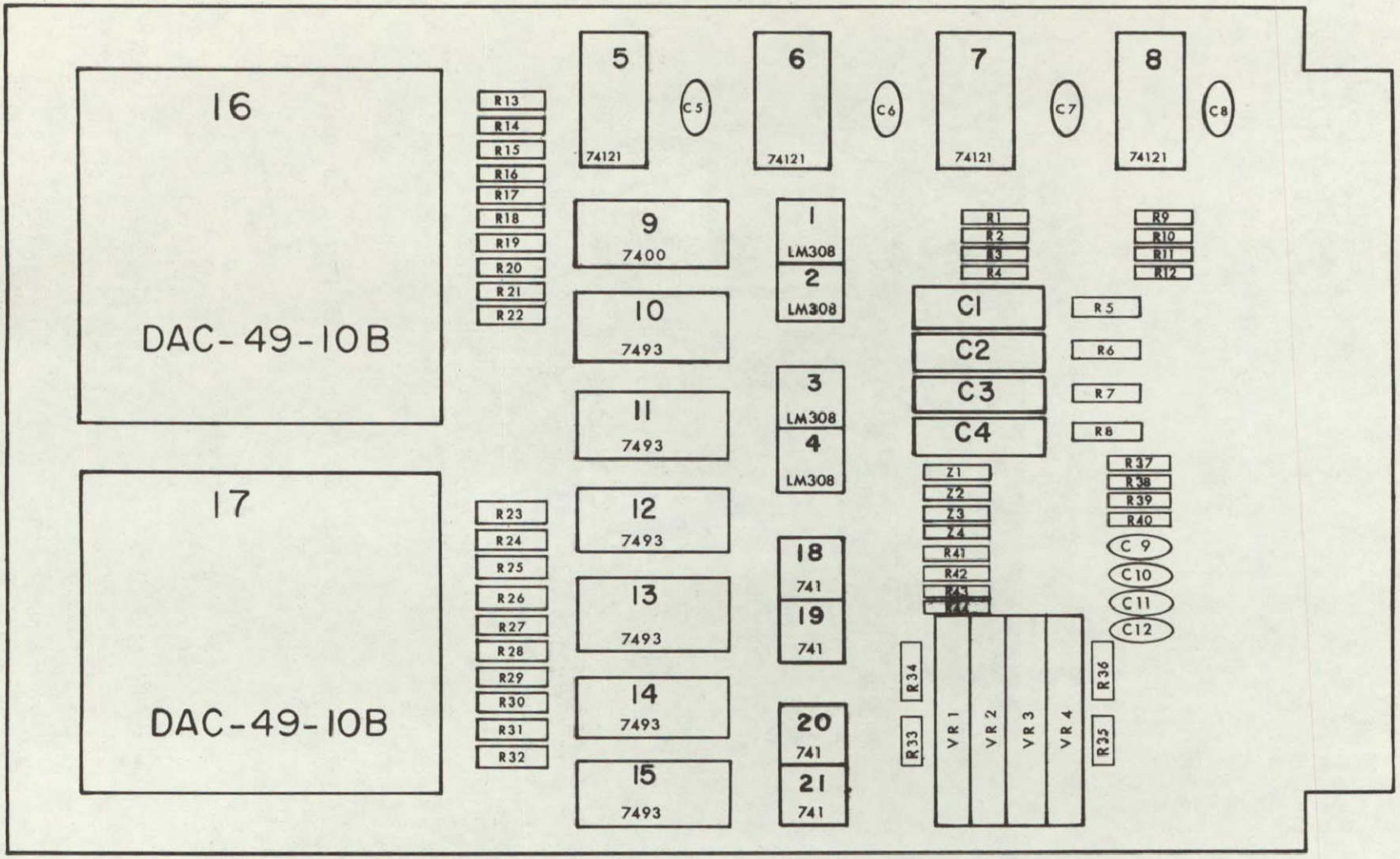

Figure 4.16 Diagram of the location of the components in the biaxial fringe counter.

3. Adjust the photodetector signal levels. Since a limiter is placed before the "one-shot," the gain after the phototransistor can be left high in most cases. The DC level of the photodetector signal does vary among fringe patterns and must usually be readjusted for each setup. Use an oscilloscope or voltmeter to monitor the analog voltage of each detector as fringes move and adjust the offset so that the voltage swings between 0 and +5 volts. If the intensity of a fringe pattern is considerably different from the previous setup, the monitored output may show no change as the fringes move; this simply means that the offset needs a large change. Fringes can be moved past the photodetector by moving the photodetector with the translation stage. If the experiment is elastic and quasi-static, the loads can be cycled to make the fringes move. This is an optimal arrangement because one can check that the indentations do not move out of the laser beam.

4.3 Specimens

4.3.1 Material Properties

The specimen material was Type 2219 aluminum 1/8 inch (3.2 mm) thick furnished by NASA-Lewis. The specimens were oriented so that the rolling direction was parallel to the loading direction. The stress-strain curve from an ASTM specimen with the same orientation is shown in Figure 4.17. This curve was obtained using an Instron test machine and foil gages on the specimen. Another specimen was instrumented with foil gages in the longitudinal and transverse directions to obtain Poisson's Ratio. From these data, the elastic properties are determined to be:

Elastic Modulus = $70 \pm 1 \times 10^3$ MPa

Poisson's Ratio = 0.33 ± 0.01

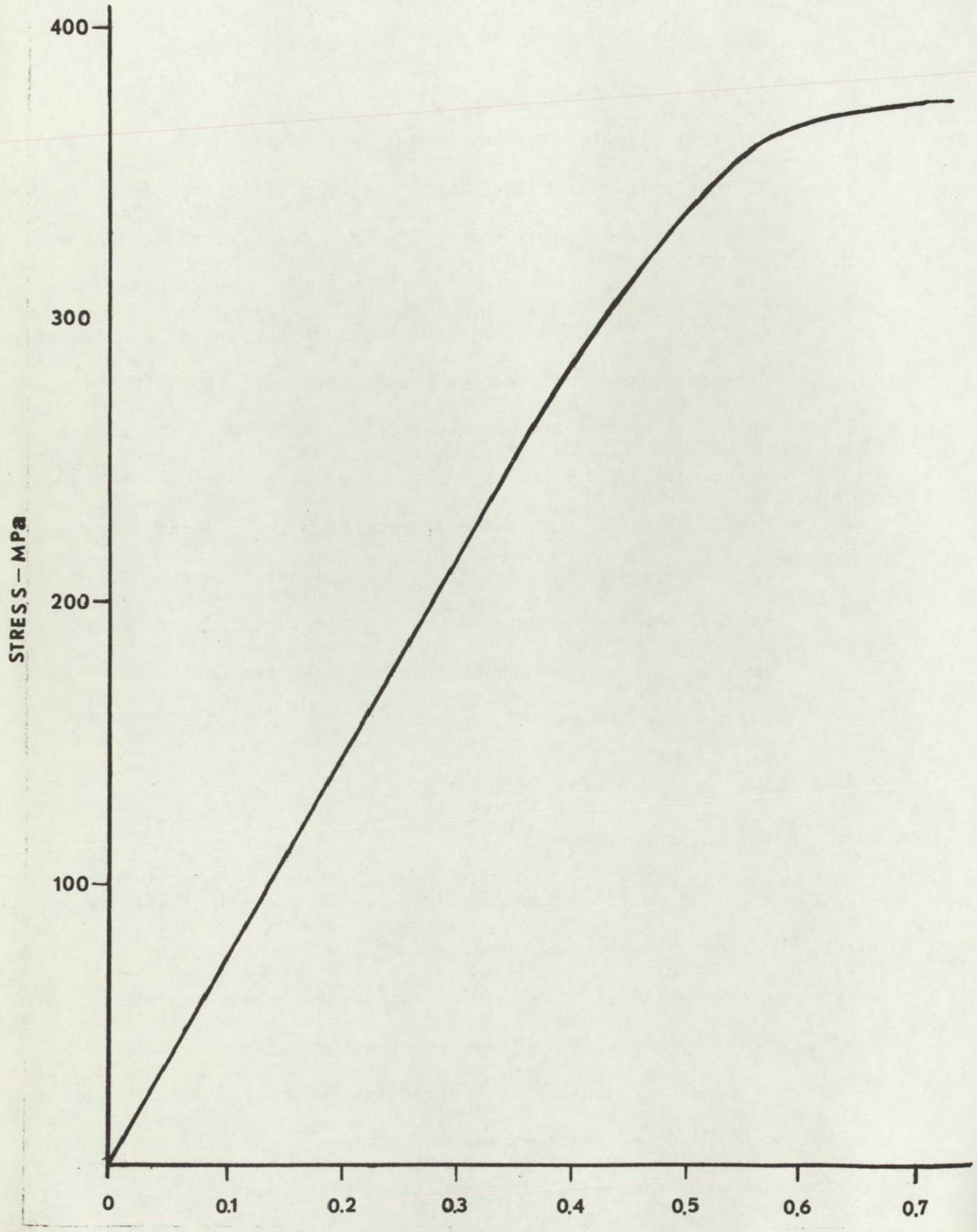

Figure 4.17 Stress-strain of Type 2219 aluminum.

4.3.2 Specimen Geometry

A schematic of the specimen is given in Figure 4.18. A slot nominally 12.5 mm long was electromachined in the sheet specimens. Six specimens were tested; each had the slot oriented at a different angle to the load direction. The thickness of the slot was measured at five positions along the slot - at the ends (X_1 and X_5), the middle (X_3) and the quarter-points (X_2 and X_4) as indicated in Figure 4.18. The data on the slot geometry are given in Table 4.1

TABLE 4.1

Slot Angle	Slot Thickness - Microns					2a - mm
	X_1	X_2	X_3	X_4	X_5	
0^o	314	314	309	364	389	12.750
15^o	291	306	284	294	292	12.806
30^o	284	282	276	313	289	12.798
45^o	285	286	291	292	290	12.793
60^o	276	282	272	290	275	12.815
75^o	231	242	228	247	240	12.742

4.3.3 Indentation Application

The indentations were applied with a Vicker's hardness tester using the 100 p weight. With this instrument, one can locate the indentations within $\pm$ 2 microns if care is taken. The specimen was first sanded with 320, 400, and 600 grit metallurgical paper and then polished with 1 micron and finally 0.3 micron alumina paste following standard metallurgical procedures. A photomicrograph of a set of indentations is in Figure 4.19a; it also shows the relative smoothness of the slot.

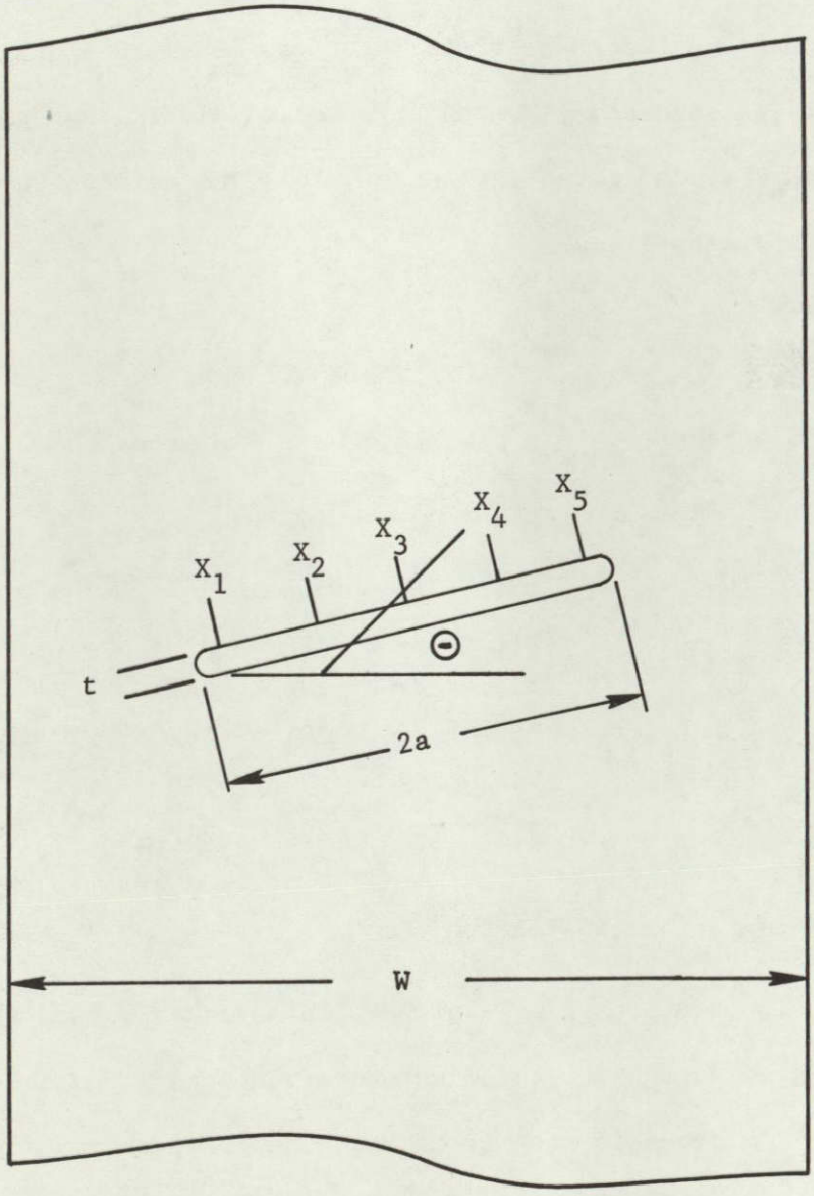

Figure 4.18 Schematic of the specimens.

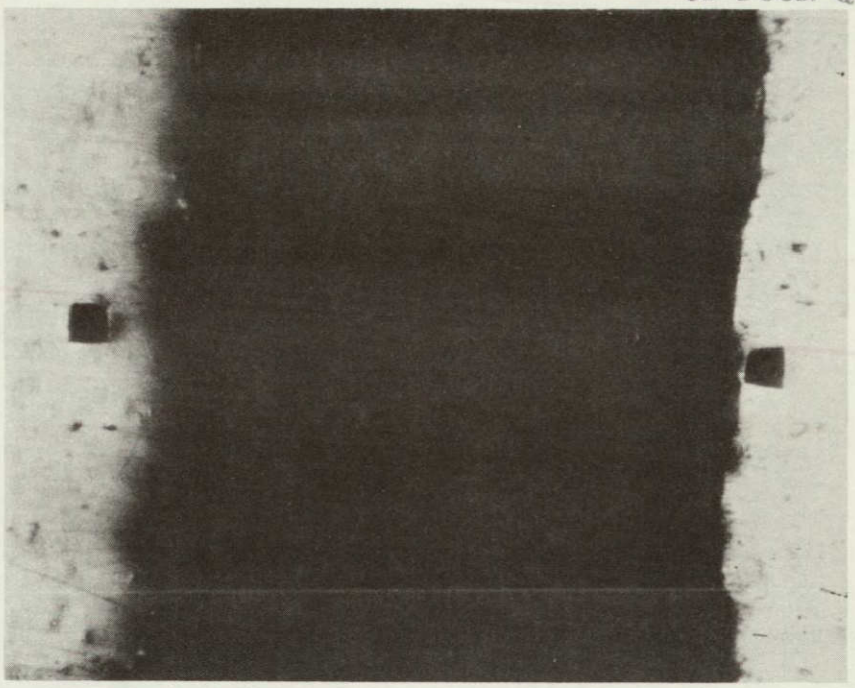

a

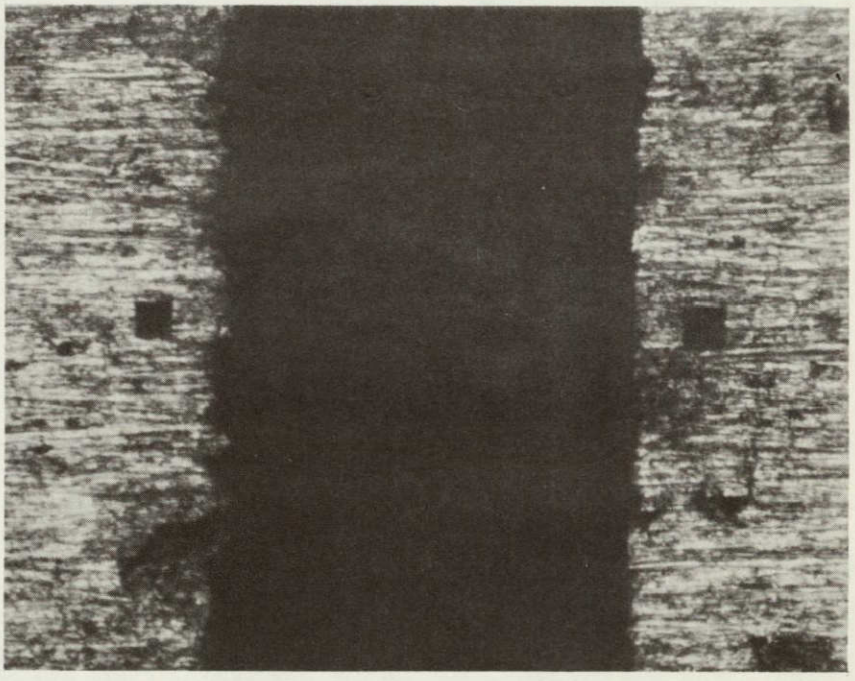

b

Figure 4.19 The slot and indentations for a specimen that has been polished (a) and one that has been sanded (b).

It was learned during the course of the work that it was unnecessary that the specimen surface be exceptionally smooth. If one stops the surface preparation after the 600 grit sanding, acceptable indentations can be applied. The trick is to align the final sanding scratches so that they are not perpendicular to the line between indentations. The laser beam reflects perpendicular to the scratches and if this reflection is oriented so that it does not interfere with the fringe patterns, then high-quality fringes can be obtained. Figure 4.19b shows a set of indentations in a sanded specimen. These give results just as good as the smoother specimen, but with less preparation time.

4.3.4 Biaxial Indentation Application

The indentations for uniaxial displacements (i.e., perpendicular to the slot) were applied directly to the specimen. As discussed in Section 4.1.2, tabs must be applied for biaxial measurements.

The tabs were cut from a Pt-Rh alloy sheet 0.010 inch (250 microns) thick with a wire saw. This material was used simply because it was available from previous work; aluminum would have been fine. The wire saw had a blade 350 microns in diameter and cutting was done with an alumina and oil paste. Better cuts can be made with a wire spark cutting apparatus, but it is very slow.

The nominal size of the tabs was to be 0.010 inch (250 microns) by 0.030 inch (750 microns) for the tab crossing the slot and 0.010 inch (250 microns) square for the other two tabs (see Figure 4.5). Variations in the cuts made with the wire saw caused some of the tabs to be slightly larger than this. A photograph of a set of tabs with indentations is in Figure 4.20. The procedure for applying tabs is:

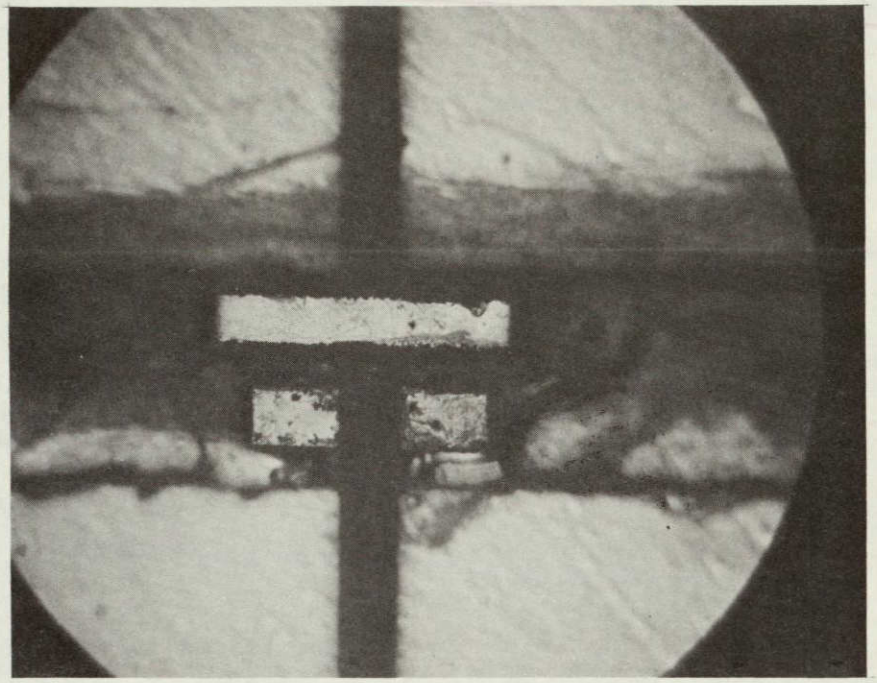

Figure 4.20 A set of tabs for biaxial displacement measurement. The slot is 290 microns wide.

1. Polish tab material.
2. Cut tabs to size and clean in acetone.
3. Mask off the area for one tab with cellophane tape. The area under the free end of the long tab crossing the slot must be coated with Teflon spray to prevent sticking of the tab.
4. Apply one tab at a time, using Eastman 910 cement and procedures similar to those for applying foil gages, i.e., hold the tab with cellophane tape.
5. Apply indentations.

Applying a set of tabs is a delicate operation. But, if a tab is in the wrong location or becomes scratched in handling, it can be chipped off and another one applied. The main difficulty experienced was failure to get enough catalyst on the specimen to form a good bond with the contact cement.

The tabs as applied in most cases lasted for all the experiments in spite of the handling associated with testing and machining of the specimens. In conclusion, the use of tabs for biaxial measurements is a feasible experimental procedure.

4.3.5 Indentation Location

The location of the indentations on each specimen are given in Table 4.2.

5. EXPERIMENTAL RESULTS

The experimental results are presented in the form of slopes of the measured displacement-stress curves for the various positions, widths, and angles.

5.1 Test Procedure

The specimens were loaded in an Instron test machine whose load cell was calibrated for each set of experiments. A very slight preload was applied to remove slack in the linkages. Figure 4.9 shows the testing machine with a specimen in place. The normal procedure was to cycle the specimen between the maximum and minimum loads several times while adjusting the incident laser beam and adjusting the offset of the photo-detectors. This adjusting operation took most of the time required for a given displacement-stress curve; the plot was obtained directly on an X-Y plotter.

All data were recorded for increasing loads only. This was justified because the maximum load was well below that required for yielding the specimens at the slot tips. Also, repeated loading plots for a set of indentations proved to be identical.

5.2 Typical Plots

A typical plot of a displacement versus load result is shown in Figure 5.1 (this is a copy of the X-Y plot - not redrawn). A straight line was drawn through the stepped curve and the slope of the line computed. Figure 5.1 is for the displacement at the center of the crack and shows a reasonably large total displacement of approximately 7 microns.

As one moves toward the end of the slot, the displacement is less, of course; a typical plot is shown in Figure 5.2. This was taken under the

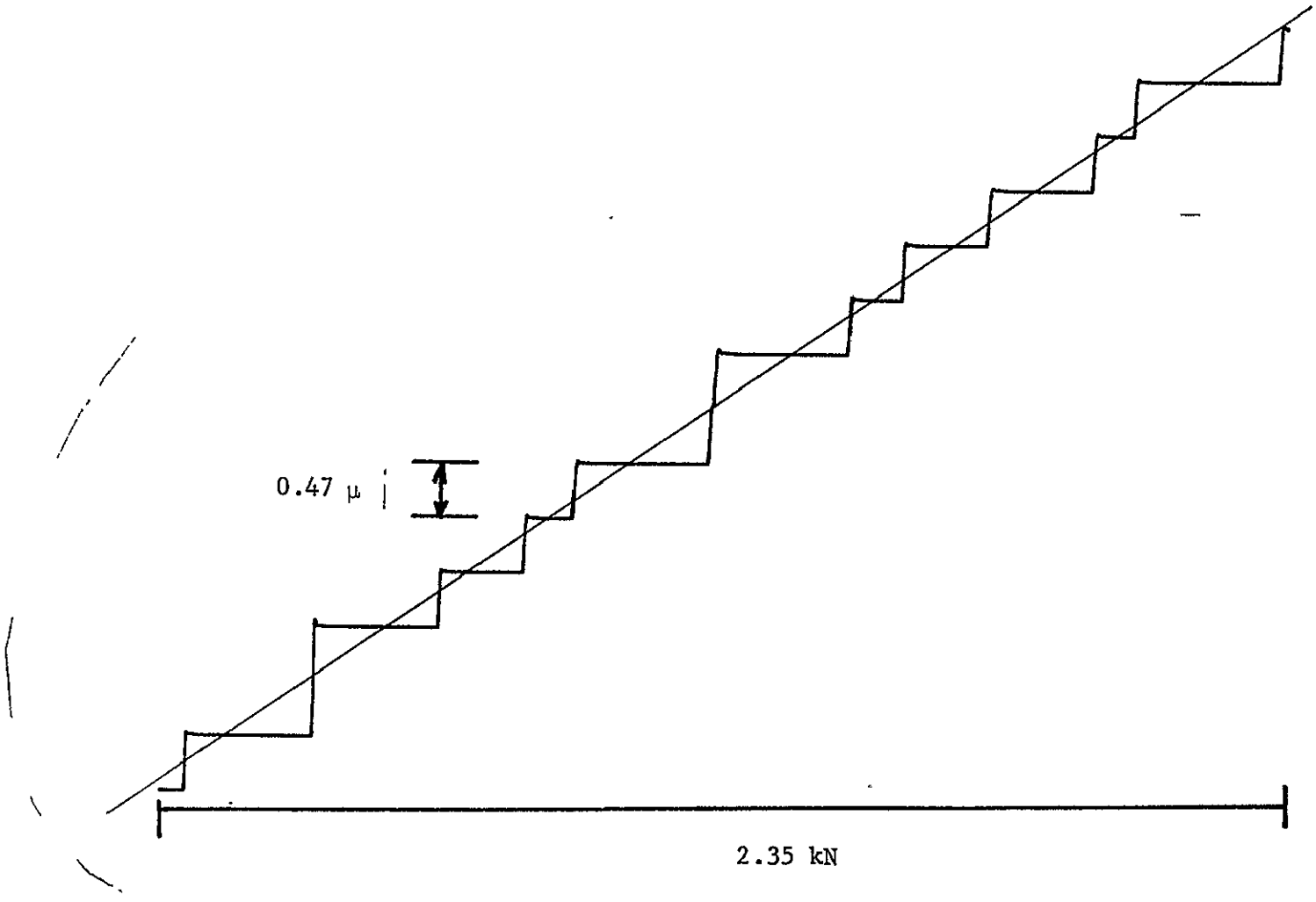

Figure 5.1 Displacement versus load at the center of the 15^{o} specimen with a/b = 0.291.

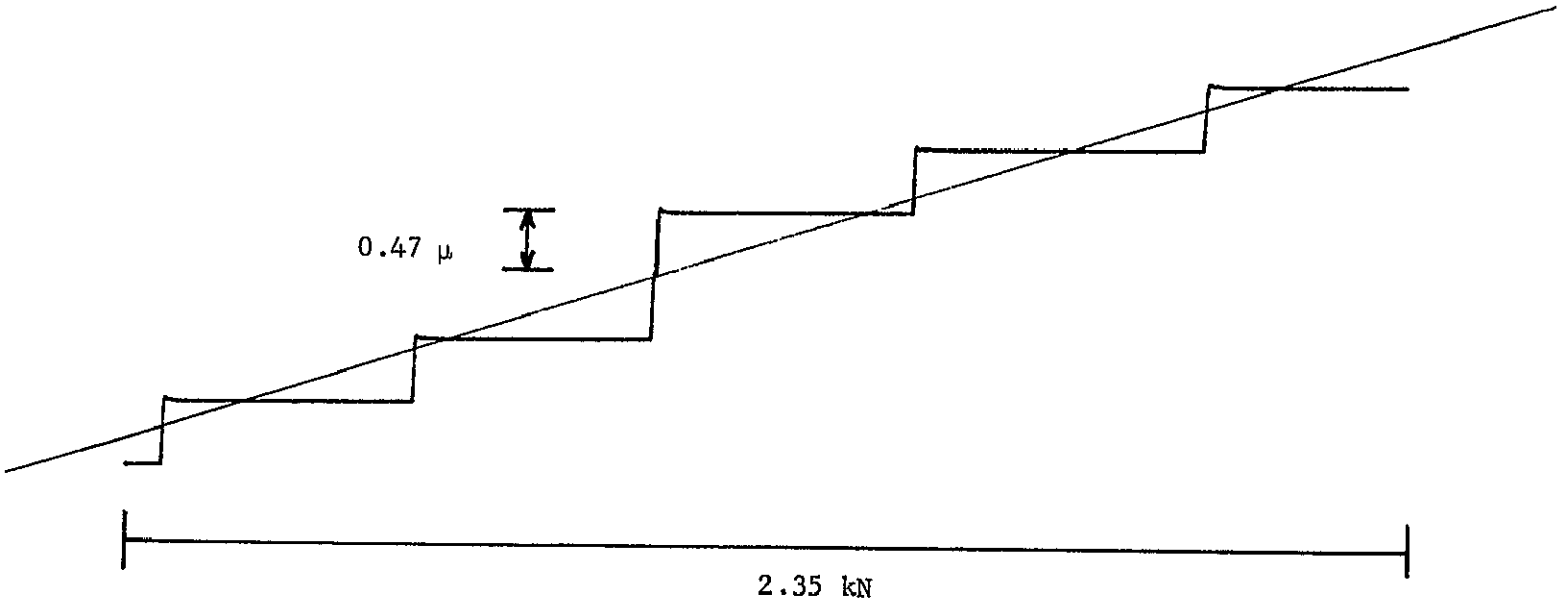

Figure 5.2 Displacement versus load at one end of the slot of the 15^{o} specimen with a/b = 0.291.

same conditions as Figure 5.1, except the displacement was measured at an end location.

When the slot angle is larger, e.g., 60^{o} or 75^{o}, the displacement at the ends of the slot become very small. They can become so small that the fringe due to displacement is smaller than that due to rigid-body motion, and one of the fringe patterns will move in a negative direction. The instrument cannot account for this; it would produce erroneous results. It becomes necessary to plot the fringe intensity as a function of applied load and manually convert this to a displacement plot. Figure 5.3 is a plot of intensities for an end location on the 60^{o} specimen. It doesn't have the cosine-squared shape of the intensity variation because of the limiter in the circuit. The upper fringe moved in a negative direction; this was determined by simply watching the fringe motion on the diode face. The locations of the maxima and minima were plotted and the displacement curve drawn as the average of these - see Figure 5.4.

5.3 Relative Uncertainties of Slopes

The uncertainty in a given slope measurement arises from the measurement technique that produces the displacement load plot and from the determination of the slope of that plot.

The relative uncertainty of the load measurement was estimated to be 1 percent; this arises mostly from the calibration procedure. The relative uncertainty of the displacement measurement is also predominantly influenced by the calibration. The calibration factor $\lambda/\sin\alpha_o$ was determined for each measurement; of course α_o is the only quantity that need be measured. Since the photodetector is approximately 40 cm from the

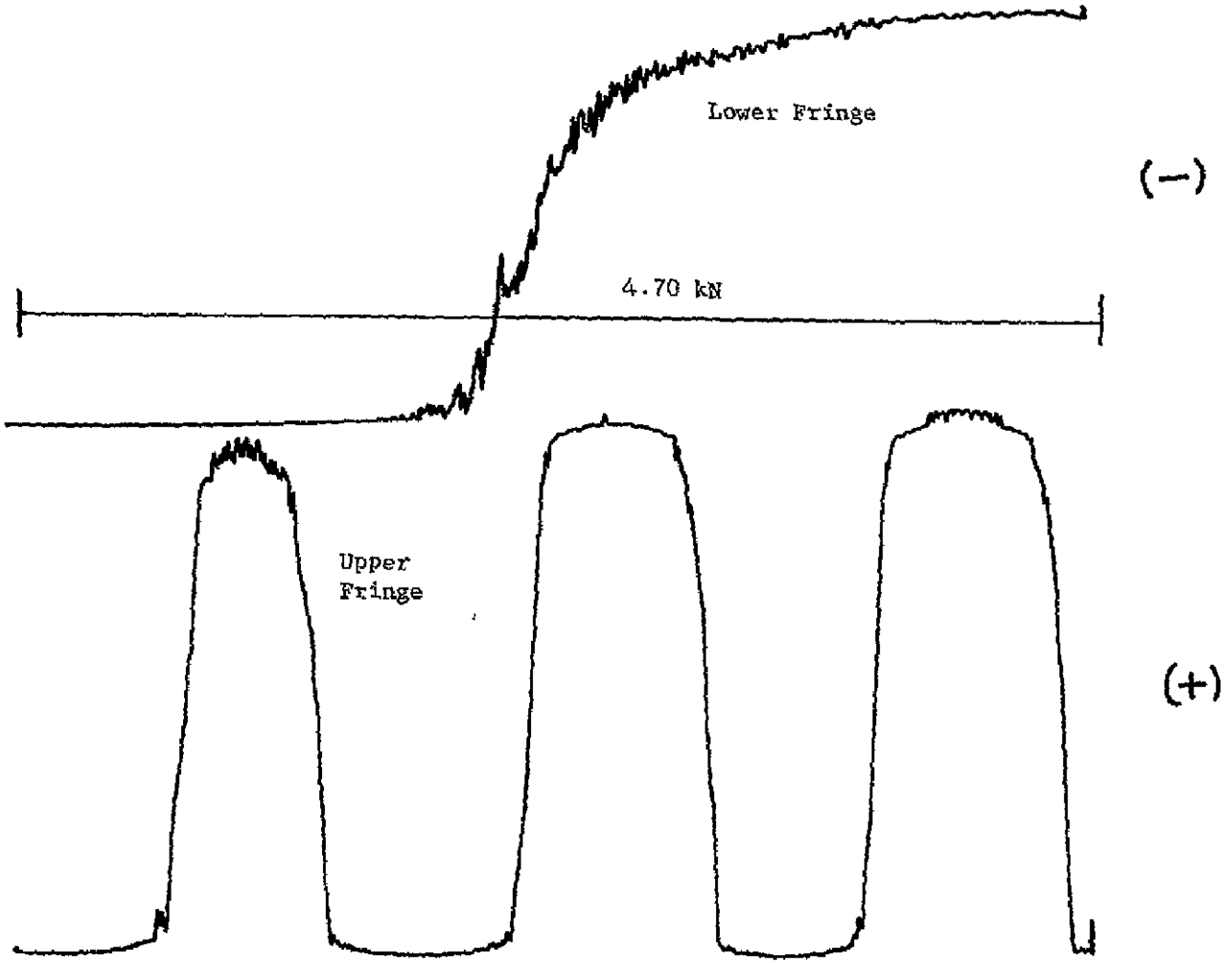

Figure 5.3 Fringe intensity versus load at one end of the slot of the 60° specimen with a/b = 0.291.

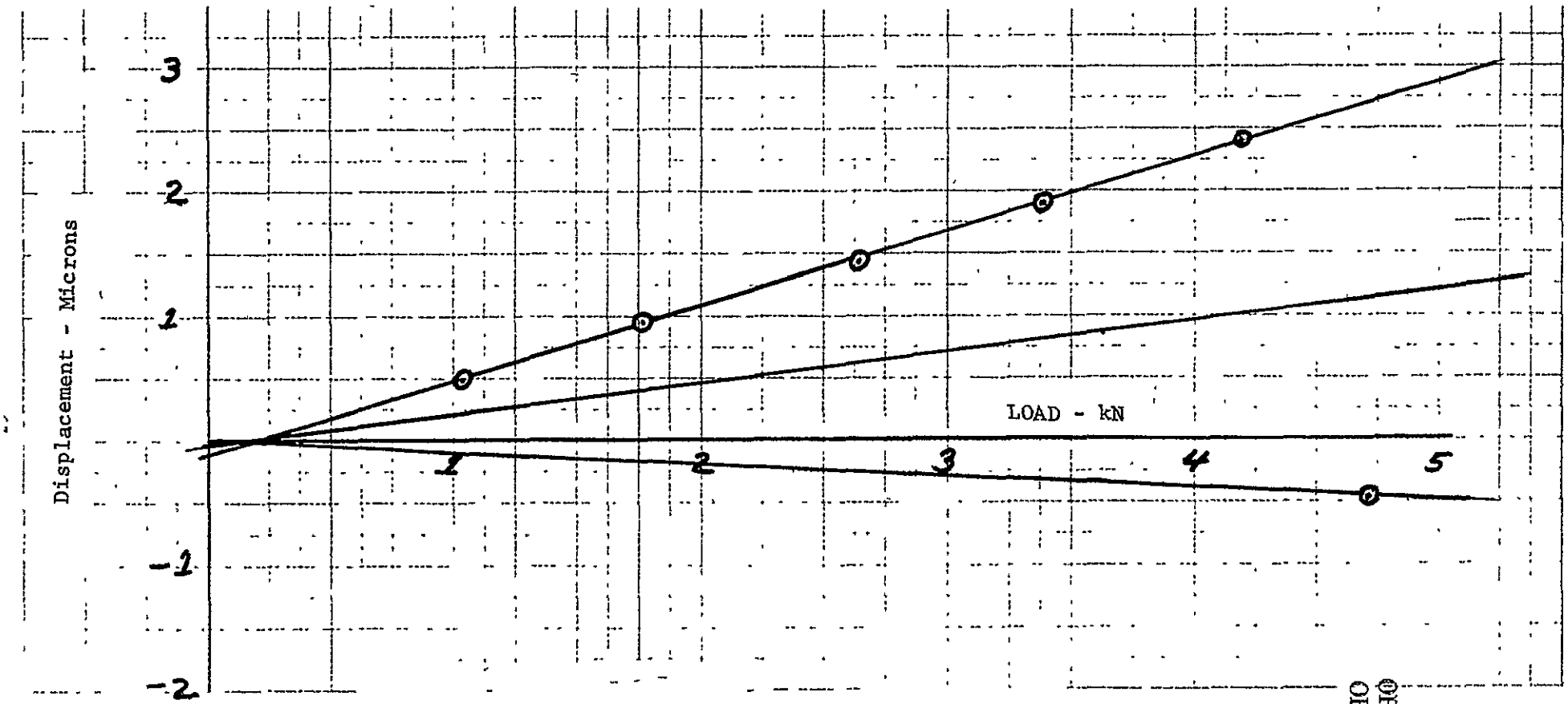

Figure 5.4 Displacement versus load data for the plot of Figure 5.3.

indentations, it is easy to measure α_o so that a relative uncertainty of less than 1 percent for $\sin \alpha_o$ is attained.

If the displacement measurement had a finer resolution, it would be easier to draw a straight line through the plot. The human element enters into where the straight line should be drawn. However, by actually drawing various straight lines (exercising normal care) and comparing the computed slopes, it was determined that the relative uncertainty of the slope calculation was also 1 percent.

It is then estimated that the relative uncertainty of a slope measurement is 3 percent.

Computation of slopes from plots showing less total displacement, e.g., Figures 5.2 and 5.3, are naturally less precise owing to the greater variability in drawing the straight line. It is estimated that the relative uncertainty of these slope measurements is 5 percent.

The instrument was developed for biaxial displacement measurements. A typical plot of the displacements perpendicular to and transverse to the crack is shown in Figure 5.5. It was recorded from the 45^o slot specimen. In running the tests it was just as convenient to record the two displacements separately, because it was hard to align the incident laser beam so that it covered all three indentations equally throughout the loading. If the laser beam was positioned primarily on two indentations, then those fringes were emphasized, i.e., the fringe patterns were "checkered," but looked more like the continuous fringe pattern from only two indentations.

5.4 Data for Horizontal Slot

The measured slopes for the horizontal slots for various widths of the specimen are plotted in Figure 5.6. Measurements were made on both

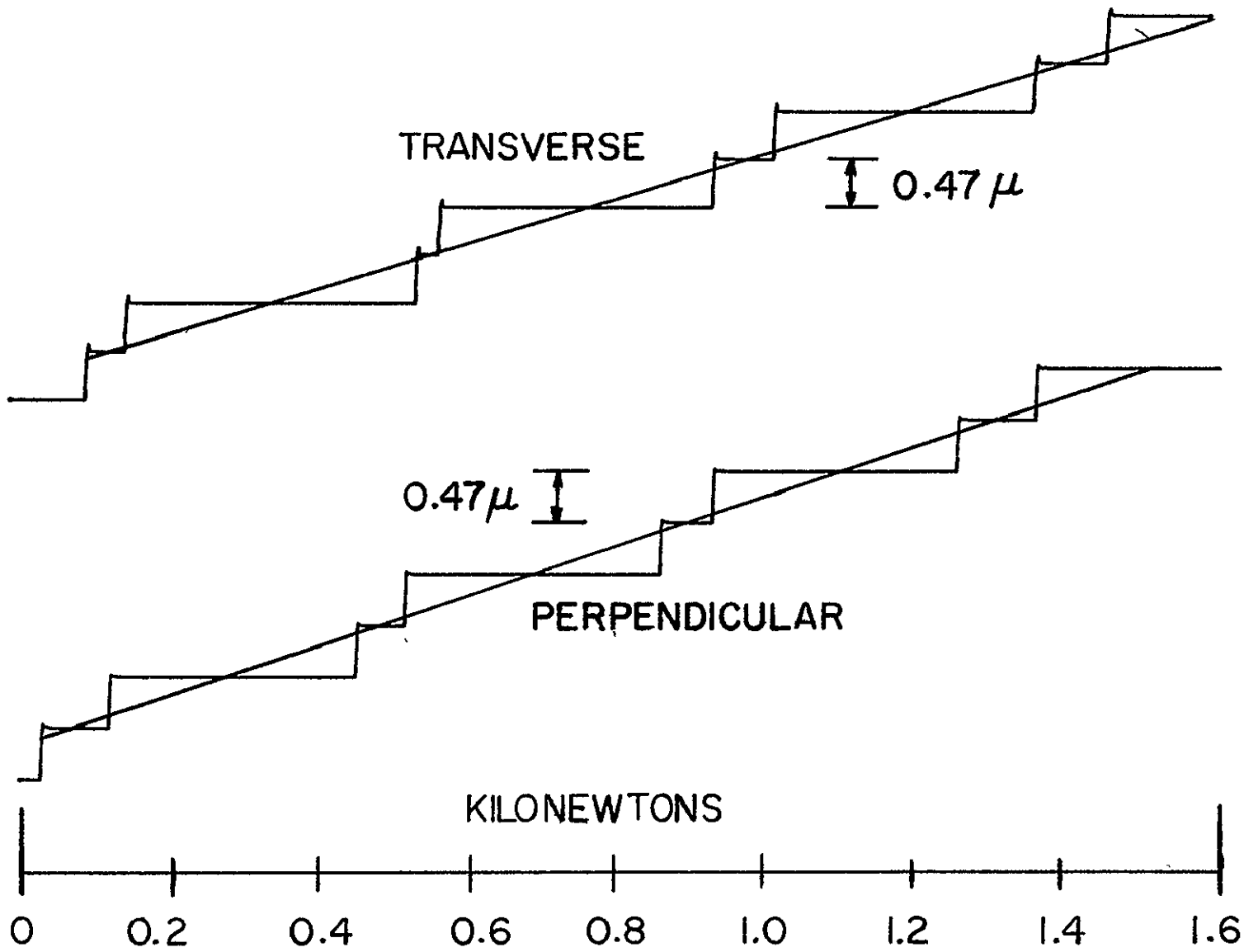

Figure 5.5 Biaxial displacement for the 45° specimen with a/b = 0.417.

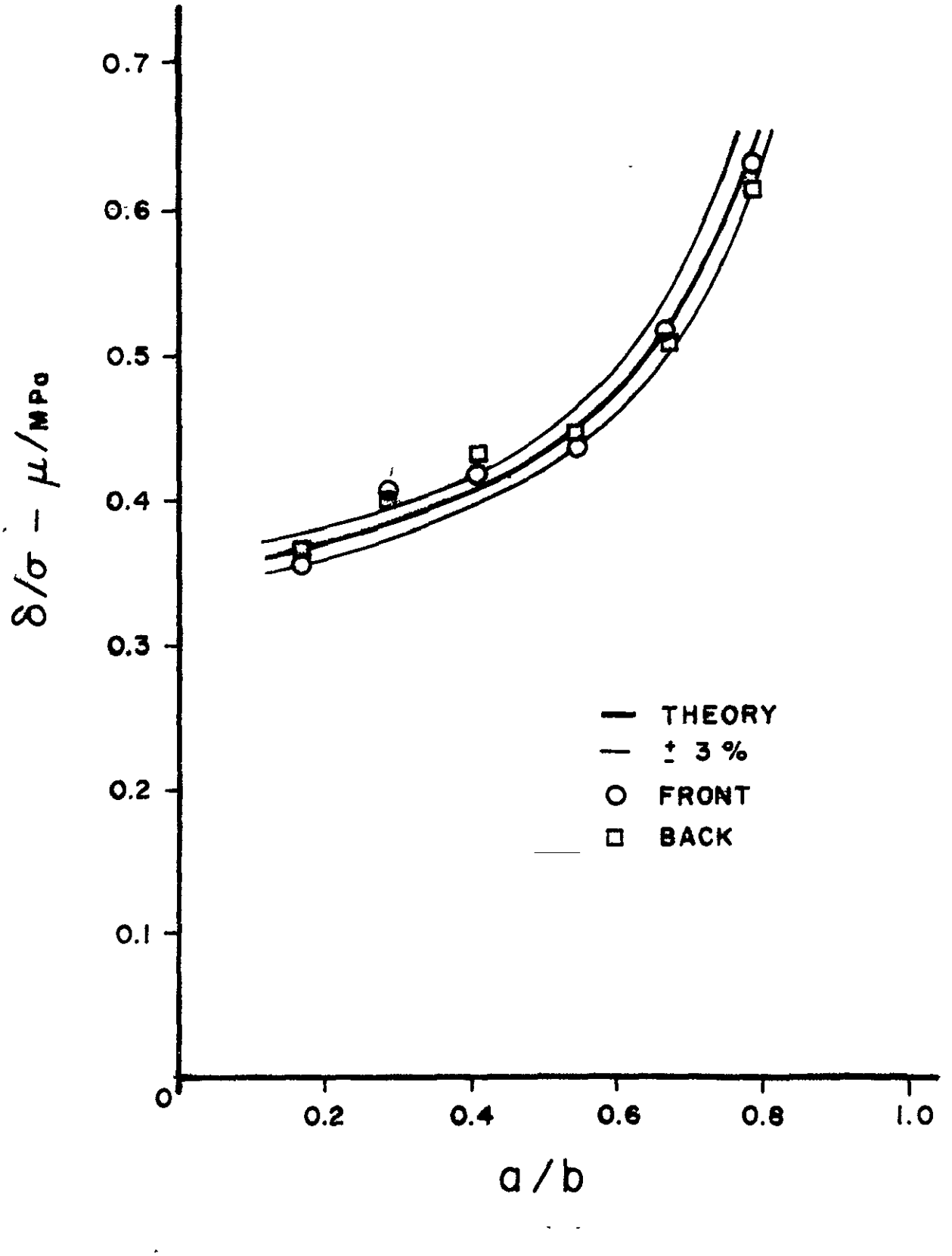

Figure 5.6 Slopes of the displacement-load plots at the center of the 0^{o} specimen.

sides of the specimen. Also plotted in Figure 5.6 are the predicted crack displacements from the formula

$$\frac{\delta}{\sigma} = \frac{4a}{E}\left[-0.071 - 0.535(a/b) + 0.169(a/b)^2 + 0.20(a/b)^3 - 1.071(b/a)\,\ell n\,(1 - a/b)\right]$$

from Reference 4, p.2.4. The thinner lines in the figure are deviations of plus or minus 3 percent from the theoretical curve. All of the measured values with the exception of the second set and one value from the third set fall within these boundaries.

Figure 5.6 is interpreted as evidence that the testing technique is valid and that the estimates of the relative uncertainty are nearly correct. The rest of the data was taken in the same fashion and is presumably just as accurate.

The displacements at the ends of the slots of the 0^{o} specimen can be predicted from the K_I value for the appropriate a/b. In Figure 5.7, the theoretical value of slope is shown as computed from an expression for K_I (Reference 4, p. 2.2, last formula) and the relation between displacement, K_I, and distance and angle from crack tip. Surprisingly good correlation is obtained - considering the fact that the slot is so wide relative to the distance of the indentations from the tip; the theory is for a thin slit. This indicates that this displacement measuring technique can be used to estimate the K_I value associated with fairly thick slots.

5.5 Displacement Data

The total matrix of displacement measurements is presented in Tables 5.1 - 5.6. It is given in the form of displacement/stress in units of microns/Megapascal x 10^{-1}. Any missing data points were usually the

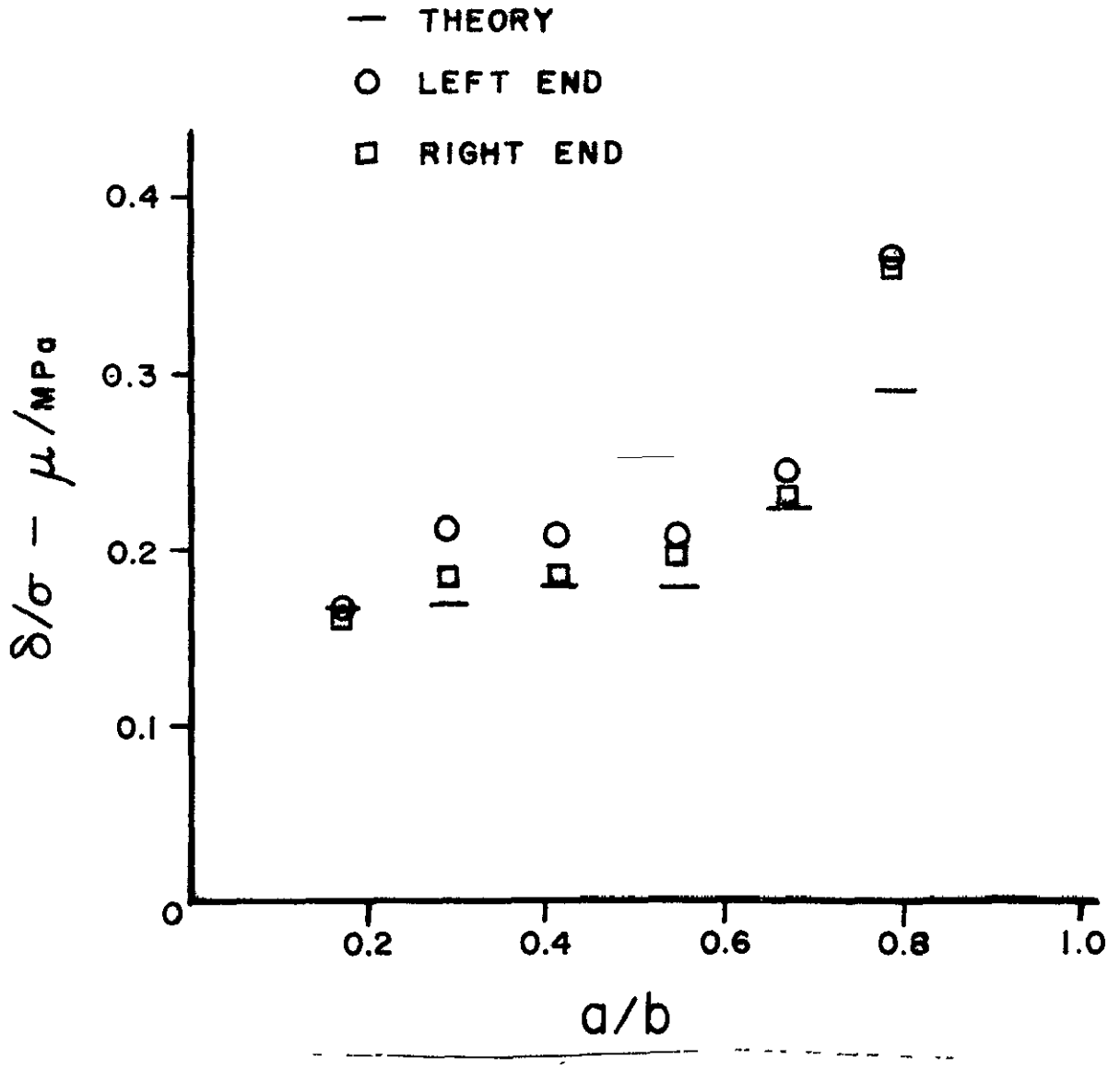

Figure 5.7 Slopes of the displacement-load plots at the ends of the 0^{o} specimen.

TABLE 5.1

Displacement/Stress (μ/MPa x 10^{-1}) for 7.62 cm Width

Slot Angle	LE	LQ	Cent	RQ	RE
			3.68 Theory		
0^{o}	1.64	3.07	3.58 Front	3.00	1.62
			3.68 Back		
			- Trans		
15^{o}	1.31	3.07	3.53 Front	2.93	1.45
			3.34 Back		
			- Trans		
30^{o}	-	2.44	- Front	2.49	0.99
			2.54 Back		
			1.60 Trans		
45^{o}	0.97	1.60	1.91 Front	1.60	0.82
			1.84 Back		
			1.60 Trans		
60^{o}	0.31	0.63	- Front	0.65	0.24
			1.16 Back		
			0.99 Trans		
75^{o}	0.09	0.19	0.22 Front	0.22	0.05
			- Back		
			0.53 Trans		

TABLE 5.2

Displacement/Stress (μ/MPa x 10^{-1}) for 4.37 cm Width

Slot Angle	LE	LQ	Cent	RQ	RE
			3.81 Theory		
0^{o}	2.11	3.52	4.06 Front	3.45	1.83
			4.04 Back		
			- Trans		
15^{o}	1.75	3.38	3.80 Front	3.22	1.68
			3.73 Back		
			0.15 Trans		
30^{o}	1.48	2.69	- Front	2.72	1.48
			2.95 Back		
			1.65 Trans		
45^{o}	0.92	1.78	2.19 Front	1.86	0.97
			2.11 Back		
			1.82 Trans		
60^{o}	0.33	0.90	- Front	0.97	0.35
			1.05 Back		
			1.28 Trans		
75^{o}	0.13	0.24	0.26 Front	0.22	0.09
			0.22 Back		
			0.46 Trans		

TABLE 5.3

Displacement/Stress (μ/MPa x 10^{-1}) for 3.05 cm Width

Slot Angle	LE	LQ	Cent	RQ	RE
			4.06 Theory		
0^{o}	2.07	3.79	4.19 Front	3.69	1.86
			4.30 Back		
			- Trans		
15^{o}	1.66	3.11	4.16 Front	3.40	1.59
			3.72 Back		
			- Trans		
30^{o}	1.34	2.63	- Front	2.69	1.28
			2.86 Back		
			1.58 Trans		
45^{o}	1.12	1.71	2.21 Front	1.91	0.90
			2.17 Back		
			2.08 Trans		
60^{o}	0.34	0.85	- Front	0.89	0.44
			1.12 Back		
			1.52 Trans		
75^{o}	0.10	0.193	0.23 Front	0.23	0.09
			0.22 Back		
			0.46 Trans		

TABLE 5.4

Displacement/Stress (μ/MPa x 10^{-1}) for 2.34 cm Width

Slot Angle	LE	LQ	Cent	RQ	RE
0°	2.06	3.81	4.48 Theory 4.39 Front 4.45 Back - Trans	3.84	1.96
15°	1.91	3.55	4.27 Front 4.14 Back 0.041 Trans	3.67	1.96
30°	1.40	2.93	- Front 3.36 Back 1.45 Trans	2.96	1.45
45°	0.91	1.97	2.36 Front 2.46 Back 1.98 Trans	1.96	1.30
60°	0.41	1.06	- Front 1.16 Back 1.56 Trans	1.01	0.46
75°	0.16	0.25	0.23 Front 0.30 Back 0.50 Trans	0.22	0.10

TABLE 5.5

Displacement/Stress (μ/MPa x 10^{-1}) for 1.90 cm Width

Slot Angle	LE	LQ	Cent	RQ	RE
			5.13 Theory		
0°	2.42	4.54	5.16 Front	4.50	2.28
			5.12 Back		
			- Trans		
15°	2.15	4.22	4.92 Front	4.24	2.17
			4.75 Back		
			- Trans		
30°	1.76	3.35	- Front	3.41	1.73
			3.78 Back		
			1.42 Trans		
45°	0.92	2.09	2.51 Front	2.19	0.95
			2.54 Back		
			1.95 Trans		
60°	0.46	1.02	- Front	1.30	0.46
			1.44 Back		
			1.62 Trans		
75°	0.11	0.34	0.34 Front	0.28	0.12
			0.34 Back		
			0.54 Trans		

TABLE 5.6

Displacement/Stress (μ/MPa x 10^{-1}) for 1.60 cm Width

Slot Angle	LE	LQ	Cent	RQ	RE
0°	3.63	5.57	6.32 Theory 6.30 Front 6.15 Back - Trans	5.34	3.61
15°	2.81	5.57	6.36 Front 6.03 Back - Trans	5.22	3.06
30°	2.08	4.34	- Front 4.99 Back 1.68 Trans	4.28	1.90
45°	1.21	2.59	3.26 Front 3.47 Back 2.19 Trans	2.90	1.21
60°	0.97	1.19	- Front 1.63 Back 1.98 Trans	1.12	1.16
75°	-	0.39	- Front 0.33 Back 0.96 Trans	0.42	-

result of displacements too small to measure. In a few cases the indentations or tabs were damaged in handling.

Figures 5.8 - 5.10 illustrate the crack shapes for different slot angles and various crack-length/specimen-width ratios. As expected, the crack opens more per unit stress for the narrower specimens and changes shape somewhat as the width changes. The crack slope (as measured by displacement perpendicular to it) remains symmetrical for the various angles and widths. This does not mean that the deformed slot is symmetrical about its axis; if the transverse displacements were measured at each point along the slot, the exact shape would be found.

Figure 5.11 shows the transverse displacements at different angles for representative length/width ratios. One would expect the transverse displacement versus angle plot to have a maximum because the transverse displacement must be zero at 0° and 90°. The experimental results indicate that the maximum is in the neighborhood of 45°.

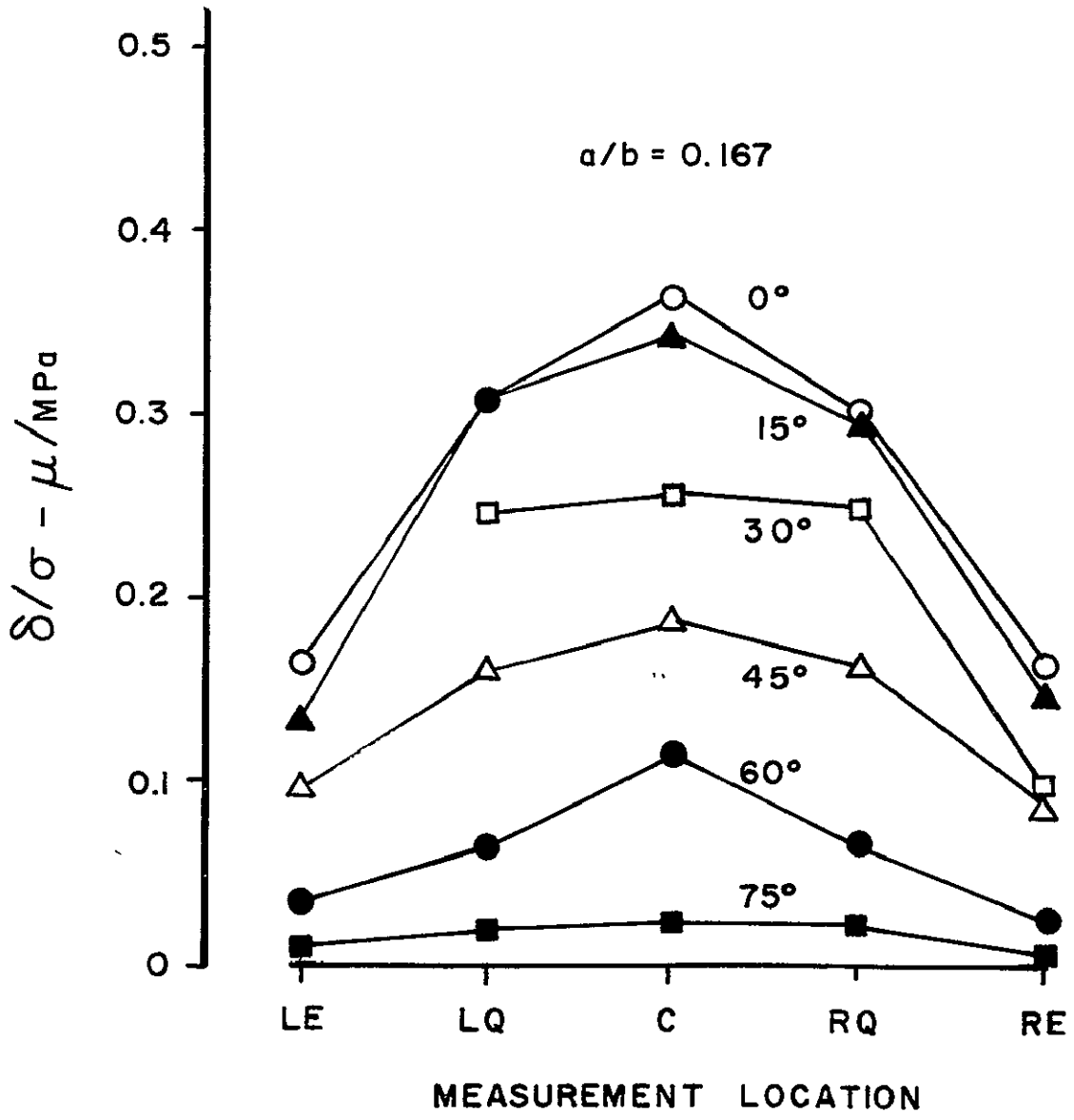

Figure 5.8 Slopes of the displacement-load plots for various angles and a/b = 0.167.

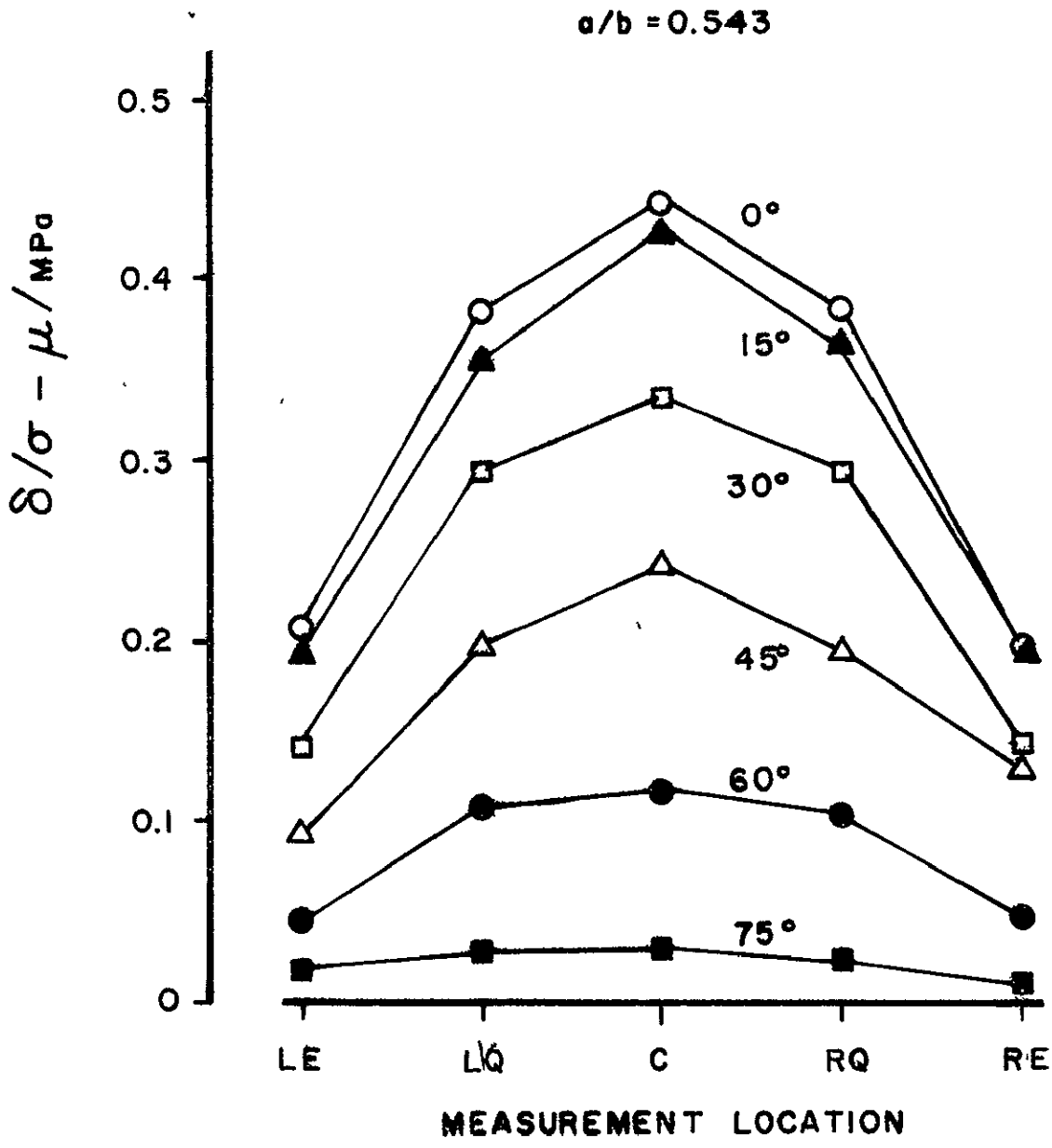

Figure 5.9 Slopes of the displacement-load plots for various angles and a/b = 0.543.

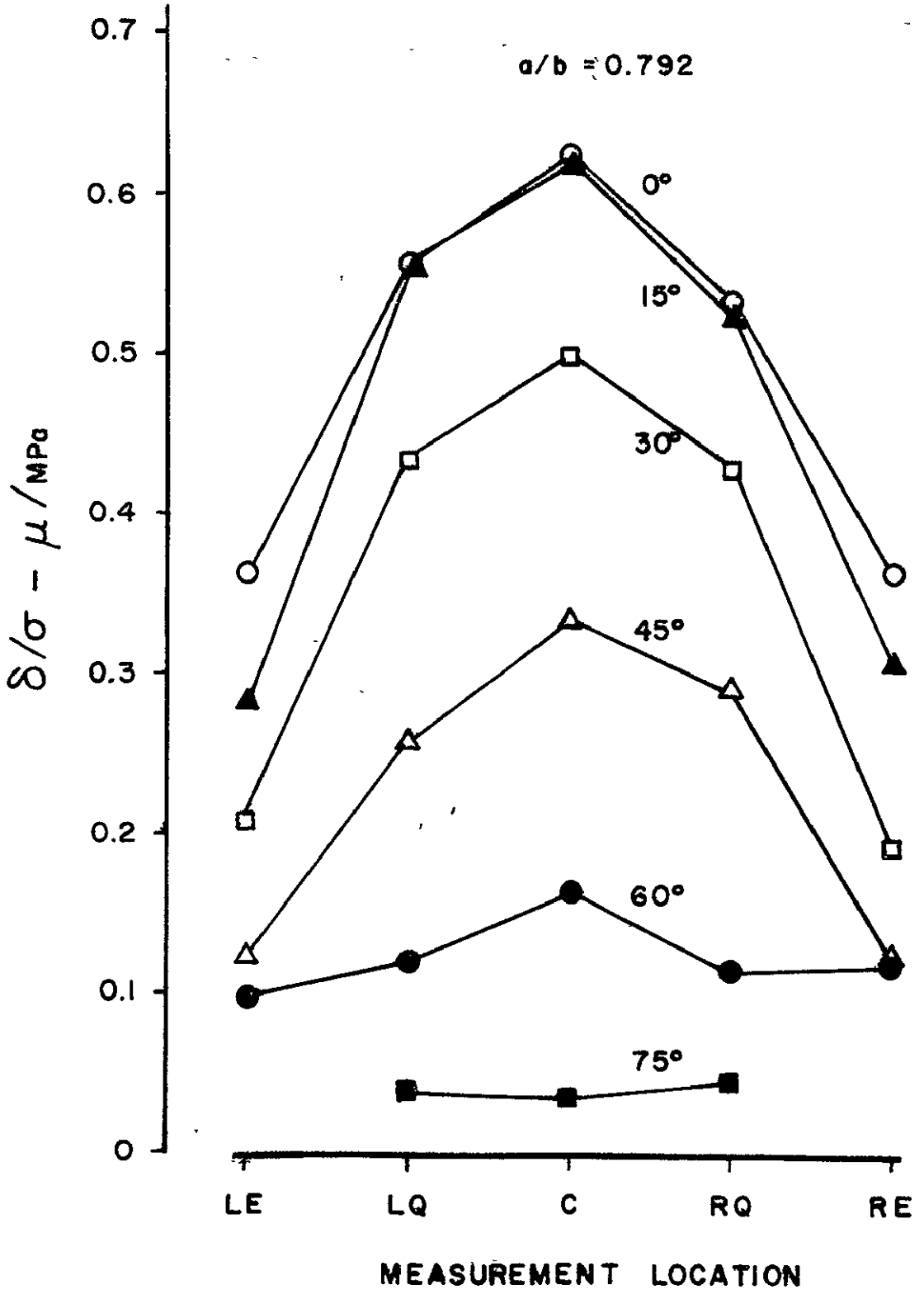

Figure 5.10 Slopes of the displacement-load plots for various angles and a/b = 0.792.

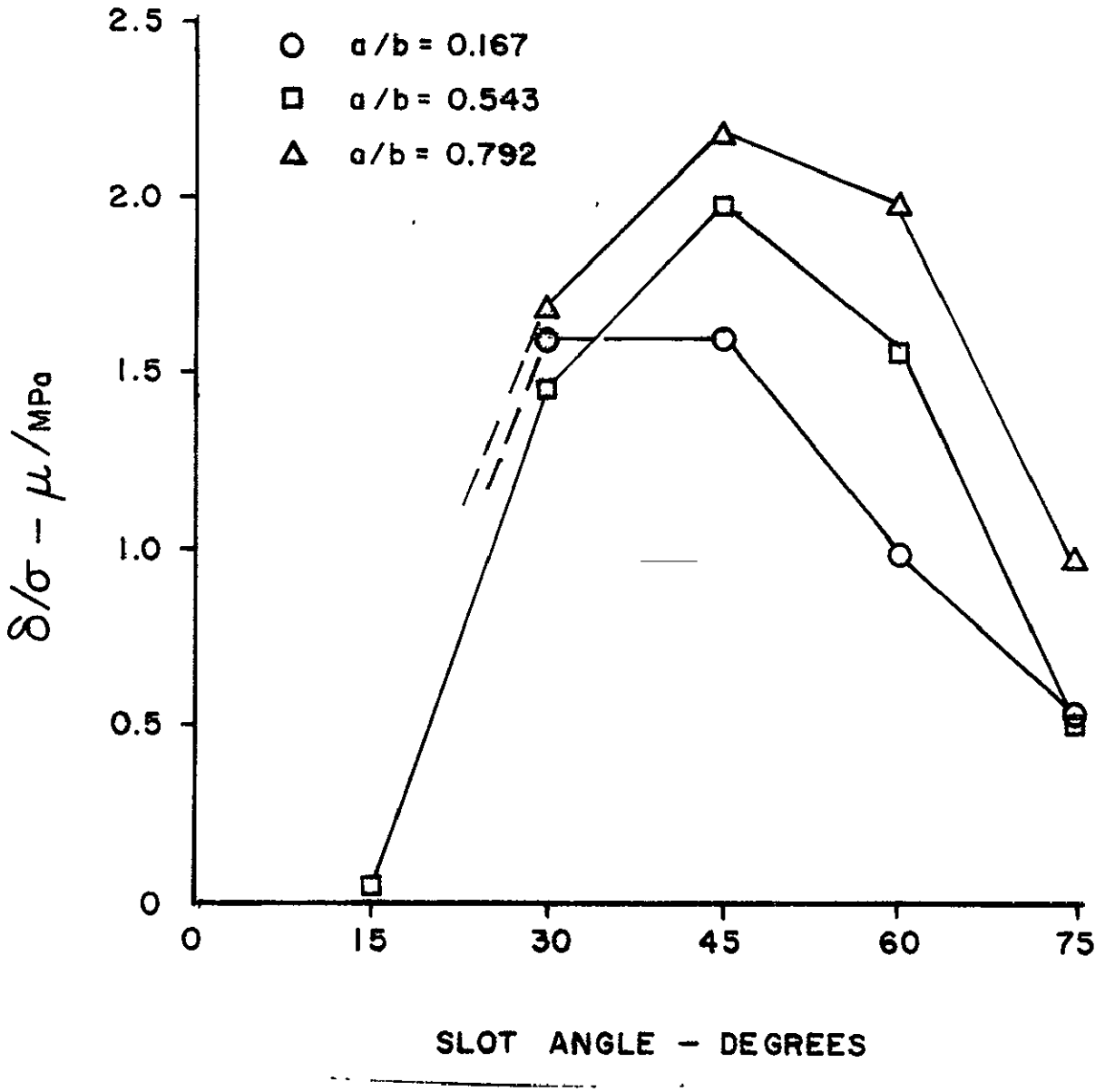

Figure 5.11 Slopes of the center transverse displacement-load plots.

6. RESULTS AND DISCUSSION

In this section, the crack surface displacements, determined by the Boundary-Integral Equation method (BIE) and by the Interferometric Displacement Gage technique (IDG), are compared and discussed.

6.1. Comparison of Results

The results obtained via the BIE method (Tables 3.1-3.6) and via the IDG technique (Tables 5.1-5.6) are again presented in Tables 6.1-6.6 for the purpose of comparison. These results are for crack opening displacements (in microns) at the center-point, quarter-point and end-point and for relative transverse displacement at the center-point. A uniaxial load of 1 MPa is assumed.

Note that the BIE results in Tables 6.1-6.6 are given in terms of the results in Tables 3.1-3.6 by

$$\delta_{center} = (u_y)_1 - (u_y)_2$$

$$\delta_{trans.} = (u_x)_1 - (u_x)_2$$

$$\delta_{quart.} = (u_y)_3 - (u_y)_4$$

$$\delta_{end} = (u_y)_5 - (u_y)_6$$

The IDG results in Tables 6.1-6.6 are simply the average of the appropriate values in Tables 5.1-5.6.

TABLE 6.1

Comparison for W = 7.62 cm.
(Displacements in microns)

Loct.	Center		Transverse		Quarter		End	
θ	BIE	IDG	BIE	IDG	BIE	IDG	BIE	IDG
0^{o}	.371	.363	.000	-	.309	.304	.080	.163
15^{o}	.347	.344	.092	-	.288	.300	.073	.138
30^{o}	.280	.254	.160	.160	.231	.247	.052	.099
45^{o}	.187	.188	.185	.160	.153	.160	.024	.090
60^{o}	.093	.116	.161	.099	.074	.064	-.003	.028
75^{o}	.024	.022	.093	.053	.016	.021	-.023	.007

TABLE 6.2

Comparison for W = 4.37 cm.
(Displacements in microns)

Loct.	Center		Transverse		Quarter		End	
θ	BIE	IDG	BIE	IDG	BIE	IDG	BIE	IDG
0^{o}	.386	.405	.000	-	.320	.349	.083	.197
15^{o}	.360	.377	.092	.015	.299	.330	.075	.172
30^{o}	.292	.295	.162	.165	.241	.271	.054	.148
45^{o}	.196	.215	.189	.182	.160	.182	.025	.095
60^{o}	.098	.105	.165	.128	.077	.094	-.003	.034
75^{o}	.025	.024	.096	.046	.017	.023	-.023	.011

TABLE 6.3

Comparison for W = 3.05 cm.
(Displacements in microns)

Loct.	Center		Transverse		Quarter		End	
θ	BIE	IDG	BIE	IDG	BIE	IDG	BIE	IDG
0^{o}	.409	.425	.000	-	.339	.374	.087	.197
15^{o}	.383	.394	.093	-	.318	.326	.079	.163
30^{o}	.312	.286	.164	.158	.257	.266	.056	.131
45^{o}	.212	.219	.194	.208	.172	.181	.026	.101
60^{o}	.107	.112	.171	.152	.084	.087	-.003	.039
75^{o}	.028	.023	.100	.046	.018	.021	-.023	.010

TABLE 6.4

Comparison for W = 2.34 cm.
(Displacements in microns)

Loct.	Center		Transverse		Quarter		End	
θ	BIE	IDG	BIE	IDG	BIE	IDG	BIE	IDG
0^{o}	.446	.442	.000	-	.371	.383	.095	.201
15^{o}	.419	.421	.093	.004	.347	.361	.085	.194
30^{o}	.343	.336	.167	.145	.282	.295	.060	.143
45^{o}	.235	.241	.200	.198	.189	.197	.027	.111
60^{o}	.119	.116	.179	.156	.092	.104	-.003	.044
75^{o}	.031	.027	.106	.050	.020	.024	-.024	.013

TABLE 6.5

Comparison For W = 1.90 cm.
(Displacements in microns)

Loct.	Center		Transverse		Quarter		End	
θ	BIE	IDG	BIE	IDG	BIE	IDG	BIE	IDG
0^{o}	.505	.514	.000	-	.424	.452	.109	.235
15^{o}	.477	.484	.093	-	.397	.423	.098	.216
30^{o}	.391	.378	.169	.142	.319	.338	.066	.175
45^{o}	.267	.253	.206	.195	.213	.214	.029	.094
60^{o}	.137	.144	.188	.162	.104	.116	-.003	.046
75^{o}	.035	.034	.112	.054	.023	.031	-.024	.012

TABLE 6.6

Comparison for W = 1.60 cm.
(Displacements in microns)

Loct.	Center		Transverse		Quarter		End	
θ	BIE	IDG	BIE	IDG	BIE	IDG	BIE	IDG
0^{o}	.600	.623	.000	-	.509	.546	.135	.362
15^{o}	.574	.620	.099	-	.483	.540	.123	.294
30^{o}	.462	.499	.169	.168	.378	.431	.078	.199
45^{o}	.311	.337	.212	.219	.245	.275	.032	.121
60^{o}	.159	.163	.197	.198	.118	.116	-.003	.107
75^{o}	.040	.033	.118	.096	.026	.041	-.024	-

The percentage differences are compiled in Tables 6.7-6.9 for the opening displacement and relative transverse displacement at the centerpoint and for the opening displacement at the quarter-point. The BIE solution is used as the basis for this comparison, i.e.:

$$\% \text{ difference} = \frac{\delta_{IDG} - \delta_{BIE}}{\delta_{BIE}} \times 100$$

TABLE 6.7

Percentage Difference: Crack Opening Displacement at Center-point

θ \ W	7.62	4.37	3.05	2.34	1.90	1.60
0°	- 2.16	4.92	3.91	- .90	1.78	3.83
15°	- .86	4.72	2.87	- 1.67	1.47	8.01
30°	- 9.29	1.03	- 8.33	- 2.04	- 3.32	8.01
45°	.53	9.69	3.30	2.55	- 5.24	8.36
60°	24.73	7.14	4.67	- 2.52	5.11	2.52
75°	- 8.33	- 4.00	-17.86	-12.90	- 2.86	-17.50

TABLE 6.8

Percentage Difference: Relative Transverse Displacement at Center-point

θ \ W	7.62	4.37	3.05	2.34	1.90	1.60
0°	-	-	-	-	-	-
15°	-	-83.70	-	-95.70	-	-
30°	.00	1.85	- 3.66	-13.17	-15.98	- .59
45°	-13.51	- 3.70	7.22	- 1.00	- 5.34	3.30
60°	-38.51	-22.42	-11.11	-12.85	-13.83	.51
75°	-43.01	-52.08	-54.00	-52.83	-51.79	-18.64

TABLE 6.9

Percentage Difference: Crack Opening Displacement at Quarter-point.

θ \ W	7.62	4.37	3.05	2.34	1.90	1.60
0°	- 1.62	9.06	10.32	3.23	6.60	7.27
15°	4.17	10.37	2.52	4.03	6.55	11.80
30°	6.93	12.45	3.50	4.61	5.96	14.02
45°	4.58	13.75	5.23	4.23	.47	12.24
60°	-13.51	22.08	3.57	13.04	11.54	- 1.69
75°	31.25	35.29	16.67	20.00	34.78	57.69

6.2 Discussion

The agreement between the theoretical results and the experimental results is, in general, excellent for all cases except at the endpoints. For example, the exact theoretical solution from reference 7 for the widest 0° specimen is 0.368 μ/MPa; the BIE computes 0.371, and the IDG measures 0.363. Clearly both the BIE program and the IDG techniques are accurate.

The fact that the two techniques don't agree for displacements near the crack tip is understandable. The BIE computations are for a sharp crack; whereas the IDG measurements were made on a finite slot. Note that the IDG values are larger. This difference is not noticeable for displacements at positions removed from the tip. Furthermore, the measured displacements at the tips are very small and thus subject to a larger experimental error. The computation of the relative displacement as illustrated in Figures 5.3 and 5.4 is not as accurate as it is for larger displacements.

Transverse displacements also agree very well except for the 15° case. In that case, the experimental values were so small as to make them suspect. This agreement shows that the elaborate technique of gluing tabs across the slot doesn't distort the measurements.

The BIE results are tainted for the cases $\theta = 60^{\circ}$ and $\theta = 75^{\circ}$ because of the negative crack opening displacements at the endpoints. This indicates that the sharp crack surfaces cross each other - a physical impossibility. By allowing this to happen, the displacements at other positions are adversely affected. It appears that for angles less than 60° this crack surface overlap doesn't occur in the BIE computations.

The relative displacements for 75° cracks show a larger percent difference between the BIE and the IDG. These measured displacements were very small and therefore subject to uncertainties as mentioned above.

The results of this extensive research program show that the theoretical and experimental techniques (both of which were developed in the course of the work) are valid for computing crack surface displacements. The choice of method for future problems will depend on how easily the geometry and applied loads can be modeled. Where external loads can be accurately predicted, the BIE method is more appropriate. For more complicated situations the IDG is an accurate, easy-to-use experimental technique.

REFERENCES

1. N. J. Altiero, and D. L. Sikarskie, "An integral equation method applied to penetration problems in rock mechanics", Boundary-Integral Equation Method: Computational Applications in Applied Mechanics (eds. T. A. Cruse and F. J. Rizzo), ASME AMD- Vol. 11, 119-141 (1975).

2. N. I. Muskhelishvili, Some Basic Problems of the Mathematical Theory of Elasticity (trans. J.R.M. Radok), Noordhoff, (1953)

3. A. Mirmohamadsadegh, and N. J. Altiero, "A boundary-integral approach to the problem of an elastic region weakened by an arbitrarily-shaped hole," submitted to International Journal of Solids and Structures.

4. W. N. Sharpe, Jr., "Interferometric surface strain measurement," Intl. J. Nondestructive Testing 3, 59-76(1971).

5. W. N. Sharpe, Jr., "A new biaxial strain gage," Review of Scientific Instruments 41, 1440-1443 (Oct. 1970).

6. W. N. Sharpe, Jr., "Dynamic strain measurement with the interferometric strain gage," Exp. Mech. 10, No. 2, 89-92 (Feb. 1970).

7. H. Tada, P. Paris, and G. Irwin, The Stress Analysis of Cracks Handbook, Del Research Corporation, Hellertown, Pa., (1973).

ACKNOWLEDGEMENTS

The authors gratefully acknowledge the support of the National Aeronautics and Space Administration, Lewis Research Center, under Grant NSG-3101. Special gratitude is extended to Dr. Thomas Orange of NASA-Lewis for his helpful suggestions and comments. Also the capable assistance of students Ali Mirmohamadsadegh, Marc Smith and Thomas Payne was most appreciated.